AGU PUBLICATIONS

JGR

Journal of Geophysical Research: Oceans

RESEARCH ARTICLE

10.1002/2013JC009452

Key Points:
- Submarine canyons are associated with deep (140–260 m) sources of upwelled water
- Canyon upwelling strength varies with along-shelf velocity at the outer shelf
- Canyon upwelling influences near-bottom water on shelf-wide and regional scales

Correspondence to:
T. P. Connolly,
tconnolly@whoi.edu

Citation:
Connolly, T. P., and B. M. Hickey (2014), Regional impact of submarine canyons during seasonal upwelling, *J. Geophys. Res. Oceans*, *119*, 953–975, doi:10.1002/2013JC009452.

Received 19 SEP 2013
Accepted 13 JAN 2014
Accepted article online 16 JAN 2014
Published online 12 FEB 2014

Regional impact of submarine canyons during seasonal upwelling

Thomas P. Connolly[1] and Barbara M. Hickey[2]

[1]Woods Hole Oceanographic Institution, Woods Hole, Massachusetts, USA, [2]School of Oceanography, University of Washington, Seattle, Washington, USA

Abstract A numerical model of the northern California Current System along the coasts of Washington and British Columbia is used to quantify the impact of submarine canyons on upwelling from the continental slope onto the shelf. Comparisons with an extensive set of observations show that the model adequately represents the seasonal development of near-bottom density, as well as along-shelf currents that are critical in governing shelf-slope exchange. Additional model runs with simplified coastlines and bathymetry are used to isolate the effects of submarine canyons. Near submarine canyons, equatorward flow over the outer shelf is correlated with dense water at canyon heads and subsequent formation of closed cyclonic eddies, which are both associated with cross-shelf ageostrophic forces. Lagrangian particles tracked from the slope to midshelf show that canyons are associated with upwelling from depths of ~140–260 m. Source depths for upwelling are shallower than 150 m at locations away from canyons and in a model run with bathymetry that is uniform in the along-shelf direction. Water upwelled through canyons is more likely to be found near the bottom over the shelf. Onshore fluxes of relatively saline water through submarine canyons are large enough to increase volume-averaged salinity over the shelf by 0.1–0.2 psu during the early part of the upwelling season. The nitrate input from the slope to the Washington shelf associated with canyons is estimated to be 30–60% of that upwelled to the euphotic zone by local wind-driven upwelling.

1. Introduction

The northern California Current System (CCS) is a region where numerous submarine canyons intersect the shelf break (Figure 1a). Upwelling-favorable wind stress during summer months is relatively weak in this part of the CCS compared with locations further south, but the presence of submarine canyons is thought to contribute to enhanced upwelling in the subsurface water column. Southward flow over the outer continental shelf, typical during summer months in the northern CCS, is associated with large vertical excursions of dense water and flow toward shore near the heads of canyons [*Hickey*, 1997; *Allen et al*., 2001]. *Hickey and Banas* [2008] estimate that the flux of nitrate across the shelf break through submarine canyons is comparable to the nitrate input into the euphotic zone by local wind-driven coastal upwelling, suggesting that submarine canyons greatly influence regional productivity. Upwelled water is also associated with low dissolved oxygen concentrations, which contributes to hypoxia in the northern CCS [*Grantham et al*., 2004; *Connolly et al*., 2010; *Crawford and Peña*, 2013].

Upwelling events near submarine canyons along the shelf break occur when the overlying flow travels opposite to the direction of coastal trapped wave propagation, which corresponds to equatorward flow in the CCS. Observations indicate that equatorward flow events are correlated with up-canyon flow and cold temperatures above the canyon [*Hickey*, 1997; *Allen et al*., 2001; *Allen and Hickey*, 2010]. Equatorward flow crosses isobaths at the upstream side of the canyon, and cyclonic vorticity is generated within the canyon as fluid columns stretch [*Allen*, 1996; *Hickey*, 1997]. As equatorward flow turns onshore, the onshore-directed pressure-gradient force becomes unbalanced [*Klinck*, 1996; *She and Klinck*, 2000]. A closed cyclonic eddy often forms several days following peak upwelling, as isopycnals relax [*Hickey*, 1997]. Anticyclonic vorticity (but not a closed eddy) is generated on the downstream side of the canyon as water is upwelled onto the shelf and fluid columns are compressed by the bottom [*Allen*, 1996; *Klinck*, 1996]. Surface flow ~100 m above the canyon is unaffected by the canyon bathymetry.

The modification of shelf flow near a shelf break canyon depends on the canyon geometry and regional currents. The response is sensitive to the direction of the flow, with greater net exchange occurring during

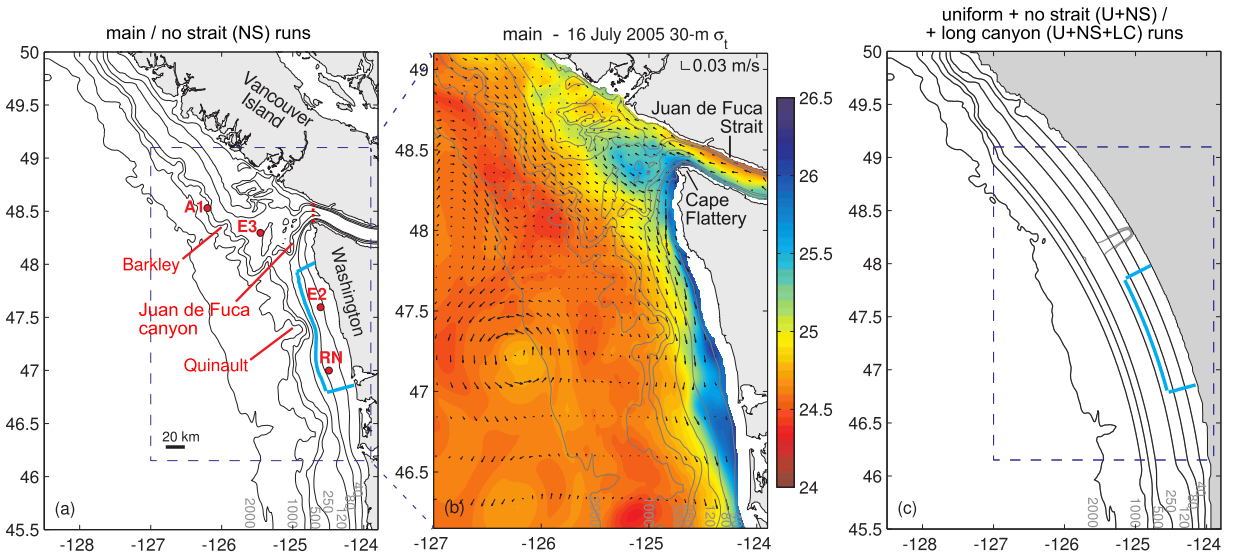

Figure 1. (a) Model domain and bathymetry for the main run and "no strait" (NS) run. Dashed red line indicates location of vertical wall at the mouth of the Strait of Juan de Fuca in the NS run. Contoured isobaths are labeled near the bottom, and contoured isobaths are smaller in shallower water. Canyons that are the focus of this study and locations of mooring observations are labeled. Dashed lines delineate the subset of the domain used for analysis. Cyan contours outline volume used for salt budgets in section 5.2. (b) Modeled density and velocity at 30 m depth on 16 July 2005. Arrows are shown for every sixth grid point. (c) As in Figure 1a, but for the "uniform + no strait" (U + NS) run and the "uniform + no strait + long canyon" (U + NS + LC) run. Bathymetry of the long canyon that intersects the uniform shelf is shown in gray.

upwelling than downwelling [*Klinck*, 1996; *Boyer et al*., 2000; *Kämpf*, 2009]. Upwelling flux increases with incident flow velocity and decreases with stratification [*Mirshak and Allen*, 2005; *Kämpf*, 2007; *Allen and Hickey*, 2010]. Theory predicts larger flux for longer and wider canyons, and canyons with sharper curvature on the upstream side [*Mirshak and Allen*, 2005; *Allen and Hickey*, 2010]. The upwelling flux is reduced in the presence of a sloping continental shelf [*Howatt and Allen*, 2013] and a turbulent bottom boundary layer [*Boyer et al*., 2006].

Compared with shelf break canyons, few studies have focused on long canyons, such as Juan de Fuca canyon (Figure 1a), which extend all the way to the coastline. Theoretical and laboratory studies suggest that long canyons with strongly converging isobaths may be locations of steady upwelling even with weak equatorward velocity over the shelf [*Allen*, 2000; *Waterhouse et al*., 2009]. Coastal trapped wave propagation is interrupted by the canyon, and upwelling through the canyon compensates for diminished equatorward flow to the north of the canyon. During strong incident flow conditions, upwelling in long canyons resembles the advection-driven upwelling of shelf break canyons [*Waterhouse et al*., 2009]. During fall and winter, *Cannon* [1972] observed mean up-canyon flow in Juan de Fuca canyon, interrupted by reversals during storm events. The up-canyon flow likely results from a combination of the barotropic cross-shelf pressure gradient associated with the equatorward upwelling jet over the shelf, and a baroclinic pressure gradient linked to the estuarine exchange flow in the Strait of Juan de Fuca [*Cannon*, 1972].

Most studies have focused on a single canyon, and only recently have model studies addressed the impact of numerous canyons on a regional scale. In the northwest Mediterranean, under downwelling conditions, *Jordi et al*. [2006] showed enhanced cross-shelf transport near submarine canyons and calculated a flushing time for the shelf on the order of 3 months. On the southern coast of Australia, *Kämpf* [2010] showed that upwelling in shelf break canyons contributes to the formation of a pool of dense, nutrient-rich water over the shelf, which can subsequently be upwelled to the euphotic zone.

Regional circulation in the northern CCS is characterized by upwelling-favorable winds and equatorward flow during spring and summer months. The seasonal cycle of upwelling-favorable wind stress peaks during summer, though downwelling and relaxation events still occur throughout this season [*Hickey*, 1979, 1998]. During summer, much of the event-scale variability is driven by coastal trapped waves generated further south [*Battisti and Hickey*, 1984]. Near-surface equatorward flow is present over the slope during April-October, but the poleward California Undercurrent (CUC) develops below shelf break depth over the slope during late summer to early fall [*Hickey*, 1979; *Thomson and Krassovski*, 2010]. The cyclonic Juan de Fuca

eddy, located offshore of Cape Flattery (Figure 1b), appears as a persistent region of dense water with 50 km horizontal scale [*Freeland and Denman*, 1982; *MacFadyen et al*., 2008]. Estuarine outflow from the Strait of Juan de Fuca, tidal currents near Cape Flattery, and variable winds are important factors in generating the Juan de Fuca eddy [*Foreman et al*., 2008; *MacFadyen and Hickey*, 2010].

In this study, a hindcast of summer 2005 in the northern CCS is used to demonstrate the effects of canyon upwelling on shelf-slope exchange in the northern CCS. This particular year is chosen in order to validate the model on a regional scale with an extensive data set from moorings and hydrographic surveys (section 3). Within shelf break canyons, the patterns and timing of modeled upwelling and vorticity are shown to be consistent with previous observational studies in the region (section 4). Two methods are used to quantify exchange between the slope and shelf over the course of the upwelling season. Lagrangian particles are tracked from the slope to the Washington midshelf, and their source depths compared for model runs with varying bathymetry and coastline (section 5.1). The salt budget for the Washington shelf is analyzed, allowing for comparison between model runs of fluxes across the shelf break and the seasonal increase in salinity (section 5.2). Finally, the implications of canyon upwelling for nutrients and dissolved oxygen are discussed (section 6).

2. Methods

2.1. Model Setup

The numerical model used in this study is an application of the Regional Ocean Modeling System (ROMS) [*Shchepetkin and McWilliams*, 2005], version 3.4. Realistic atmospheric forcing and oceanic boundary conditions are used to create a hindcast of 2005 for the domain 45.5°N–50°N, 128.5°W–123.8°W (Figure 1a). Horizontal grid spacing ranges from 1 km on the southern British Columbia shelf to 5 km near the southeast corner of the model domain, as in *Foreman et al*. [2008]. Model bathymetry over the entire domain is derived from the gridded Cascadia data set [*Haugerud*, 2000], which has 250 m horizontal resolution. The model has 20 vertical levels and uses the stretching functions of *Song and Haidvogel* [1994] with $\theta_S = 5.0$ and $\theta_B = 0.8$. Minimum depth is set to 3 m in order to avoid drying of grid cells. Bathymetry is smoothed to reduce errors in the calculation of pressure gradients near steep topography. The topographic stiffness parameter $r_0 = |\Delta h|/2h$, where h is the water depth [*Beckmann and Haidvogel*, 1993], has a maximum value of 0.24. The smoothed bathymetry retains Barkley, Juan de Fuca, and Quinault canyons (Figure 1a), which are located where model resolution is relatively high with <2 km grid spacing in both directions.

The model is initialized at the start of the year, and analysis focuses on 1 May-15 October 2005, a period when an extensive array of shipboard and moored data are available for model validation. The ocean surface is forced with six-hourly winds from a regional atmospheric model [*Mass et al*., 2003]. Additional variables from this atmospheric model are used to calculate surface heat flux using bulk algorithms [*Fairall et al*., 2003]. Evaporation and precipitation are not included. A composite of three hindcast models from 2005 is used for initial and boundary conditions of tracers and subtidal velocity. At the southern boundary, daily output from the Navy Coastal Ocean Model of the California Current System (NCOM-CCS) is used [*Shulman et al*., 2003]. At the northern boundary, which is further north than the extent of the NCOM-CCS model domain, global NCOM is used [*Kara et al*., 2006]. The western boundary of the composite uses both NCOM models, transitioning between the two at 47.5°N–48.8°N. In order to generate estuarine exchange flow in the Strait of Juan de Fuca without modeling the smaller-scale flow in Puget Sound and the Strait of Georgia, low-pass filtered output from a 2005 version of the model described by *Sutherland et al*. [2011] is used at the eastern boundary. The Columbia River is not included since the river plume effects are generally confined to the upper 20 m [*Hickey et al*., 2005], shallower than the focus of the present study. In addition to the subtidal fields described above, amplitude and phase for the K1, M2, O1, and S2 tidal constituents from a tidal model of the northeast Pacific [*Foreman et al*., 2000] are used on the boundaries.

The 3-D equations are solved using a 60 s internal time step and 2 s external 2-D time step. Advection of tracers and momentum are calculated using a third-order upstream scheme in the horizontal direction and a fourth-order centered scheme in the vertical. Bottom stress is calculated using a quadratic drag law with a nondimensional coefficient of 3×10^{-3}. Vertical mixing is parameterized using the generic length-scale turbulence closure scheme of *Umlauf and Burchard* [2003], with stability function constants from the "A" model of *Canuto et al*. [2001]. Boundary conditions for barotopic velocity and sea surface height are described by

Flather [1976] and *Chapman* [1985], respectively. Radiation conditions for baroclinic velocity and tracers are combined with adaptive nudging to all subtidal fields near the model boundary [*Marchesiello et al*., 2001]. At the open boundaries, nudging time scales are 45 days for outgoing signals and 0.125 days for incoming signals. In the model interior, time scales for nudging increase exponentially from 45 days at the boundary to 60 days over a distance of six grid points. There is no nudging further in the interior of the model domain.

2.2. Model Experiments

Experiments are used to explore sensitivity of modeled circulation to coastline and bathymetry. Forcing and boundary conditions are identical to those described above for all model runs. In one experiment, the entrance to the Strait of Juan de Fuca is replaced with a closed vertical wall at Cape Flattery. In a second experiment, shelf bathymetry between 46°N and 49°N is replaced with "uniform" bathymetry where isobaths are defined by radial coordinates (Figure 1c):

$$z = -1500 + 1450 \tanh\left(\frac{R - R_0}{16}\right), 0 \le (R - R_0) \le 25 \text{ km}, \quad (1)$$

$$z = z_0 + z_0\left(\frac{R - R_0 - 25}{55}\right), (R - R_0) > 25 \text{ km}, \quad (2)$$

where z is depth in m, R is radius in km, $z_0 = -172$ m is the depth of the shelf break, and $R_0 = 560$ km. The center of the radial coordinate system is determined by fitting a circle to the 500 m isobath. This uniform bathymetry transitions to the original bathymetry over an along-shelf distance of 25 km at 46°N and 40 km at 49°N. In a third experiment, this uniform bathymetry is further modified by adding a long canyon that extends to the coast (Figure 1c). The canyon is designed to resemble Juan de Fuca canyon, with maximum depth 250 m, 22 km width near the mouth at rim depth (∼150 m) and 10 km width at the base. All grids in the model experiments are smoothed in the same manner as the main run.

2.3. Particle Tracking

Particle pathways are computed using the Lagrangian TRANSport model [*North et al*., 2008]. In order to focus solely on the effects of advection, vertical and horizontal diffusion are set to zero, which is consistent with other Lagrangian studies of upwelling in the northern CCS [*Rivas and Samelson*, 2011] and regional impacts of submarine canyons elsewhere [*Kämpf*, 2010]. A 60 s time step is used for calculating particle trajectories from hourly model output. Particles are released at locations over the slope from the 250 m isobath seaward to 10 km, with 5 km spacing, between 46.4°N and 49.0°N. Release depths range from 40 to 400 m, at 20 m intervals. Particles are released daily during the time period April-September and tracked for 15 days.

2.4. Observations

Observations from four moorings and five shipboard surveys during the period April-October 2005 are used to validate the model (see Figure 1a). Moored sensor data are used from E2 over the 47 m isobath, RN over the 70 m isobath, E3 over the 127 m isobath, and A1 over the 500 m isobath. Velocity was measured at E2, RN, and E3 with downward-looking 300 kHz Workhorse Acoustic Doppler Current Profilers (ADCPs, Teledyne RD Instruments). At E2, hourly ensembles were obtained at 12–40 m with 2 m bin spacing. At RN, hourly ensembles were obtained at 3–63 m with 2 m bin spacing. At E3, hourly ensembles were obtained at 12–106 m with 2 m bin spacing. At A1 during this time period, velocity was measured using Aanderaa RCM8 current meters at 34, 102, and 301 m. The ADCP data are filtered with a cosine-Lanczos filter with half power point of 46 h and decimated to 6 h intervals. Each time series is rotated according to the principle axis of the depth-averaged velocity such that u is cross-shelf, positive toward shore, and v is along-shelf, positive in the poleward direction. The A1 velocity data are filtered using a Kaiser filter with 30 h cutoff, decimated to daily intervals, and rotated to the local isobath orientation (25° counter-clockwise). Temperature and conductivity measurements from 7 to 8 m off the bottom at E2 and E3 were collected using a SBE37 sensor (Seabird Electronics) at 15 min intervals. Data are averaged to hourly values, low-pass filtered, and decimated in the same manner as the ADCP data.

Shipboard profiles of temperature and salinity over the shelf and slope of Washington and British Columbia are compiled from five cruises throughout spring and summer 2005 (>200 stations, maximum profile depth

500 m). On 19 April, data were collected using a SBE19 sensor on a cross-shelf transect at 46°50′N as part of the Olympic Region Harmful Algal Bloom (ORHAB) project. Larger-scale surveys of the Washington and British Columbia shelves were conducted during two cruises (8–27 July, 5–21 September) as part of the Ecology and Oceanography of Harmful Algal Blooms-Pacific Northwest (ECOHAB-PNW) project. Data for the Washington coast were also collected during two cruises (29 May-20 June, 5–26 August) as part of the River Influences on Shelf Ecosystems (RISE) project. ECOHAB-PNW and RISE profiles were collected using SBE16*plus* sensors. All shipboard profile data are averaged at 1 dbar intervals.

3. Regional Circulation and Model Validation

In this section, the accuracy of the modeled circulation is evaluated using the extensive set of observations from 2005 in order to demonstrate the strengths and weaknesses of the model. During this season, local wind stress transitions to equatorward over 1 month later than usual in late May [*Hickey et al*., 2006; *Kosro et al*., 2006]. Remote wind forcing contributes to equatorward flow over the shelf during late May to mid July, and local wind forcing has a greater influence on shelf currents later in the upwelling season [*Connolly et al*., 2014].

3.1. Validation Statistics

Several metrics are used to quantitatively summarize model skill. The correlation coefficient (CC) indicates how well the model accounts for intraseasonal fluctuations in the observed time series. Because many of the time series have seasonal trends, the correlation coefficient of the detrended time series (CC_{DT}) is shown here. Significance levels are determined using effective degrees of freedom [*Emery and Thomson*, 2004, pp. 260]. The root-mean-squared error (RMSE) is used to quantify the overall model error for each location and variable. $RMSE = (\langle (m-o)^2 \rangle)^{1/2}$, where o is an observation, m is a corresponding model variable, and $\langle\rangle$ denotes an average. The RMSE has units of the measured variable, and is comprised of three components, $RMSE^2 = MB^2 + SDE^2 + CCE^2$, where $MB = \langle m \rangle - \langle o \rangle$ is the mean bias, $SDE = SD_m - SD_o$ is the standard deviation (SD) error, and $CCE = [2SD_m SD_o (1-CC)]^{1/2}$ is the correlation error. *Willmott* [1981] defines a skill metric that normalizes the RMSE

$$WS = 1 - \frac{RMSE}{\langle (|m-\langle o \rangle| + |o-\langle o \rangle|)^2 \rangle}, \tag{3}$$

which varies from zero to one. WS is used to compare overall performance between different modeled variables and different models.

3.2. Time Series

Time series observations over the shelf span the period May-September 2005, allowing for an evaluation of model performance at time scales of weather events (~2–10 days) and variability in velocity and water properties over several months. To compare with a larger-scale, coarser-grid model, time series from the NCOM-CCS model are also extracted from the adjacent model grid points with the closest bottom depths.

3.2.1. Velocity

Modeled depth-averaged velocity is significantly correlated with observations at all locations over the shelf (Table 1 and Figures 2a, 2c, and 2e). The E2 location is relatively shallow, and is therefore strongly influenced by local wind stress. Despite the relatively high correlation, this location has the strongest mean bias of -0.05 m s^{-1} (Table 1 and Figures 2b, 2d, and 2f), likely due to an equatorward bias in the MM5 winds [*Tinis et al*., 2006]. Over midshelf at RN (Figures 2c and 2d), the correlation is weaker than at E2 and the WS metric indicates that skill is less than that for the NCOM-CCS model. Variability at midshelf in this region is strongly influenced by remotely generated coastal trapped waves [*Battisti and Hickey*, 1984], suggesting that the smaller WS in the model used here is likely due to problems with nudging at the open boundaries. Despite the weaker correlation with observations at this location, the timing and magnitude of the strongest equatorward flow during mid July, and the mean vertical structure, are similar to the observations (Figures 2b and 2d). In deeper water offshore of Cape Flattery at E3, modeled variance is weaker than the observed variance (Figure 2), similar to midshelf. However, the model shows an overall improvement over NCOM-CCS at this location (Table 1). This location is influenced by the outer limb of the Juan de Fuca eddy (Figure 1b), a

Table 1. Model-Observation Statistics[a]

Site	Variable	Depth	CC_{DT}	WS	WS_{NCOM}	RMSE	MB	SDE	CCE
E2	*V*	Avg.	**0.78**	**0.83**	0.82	0.10	−0.05	−0.04	0.08
RN	*V*	Avg.	**0.52**	0.69	0.81	0.08	−0.02	−0.02	0.07
E3	*V*	Avg.	**0.46**	**0.72**	0.60	0.06	−0.01	−0.01	0.06
A1	*V*	35 m	0.24	**0.72**	0.36	0.11	−0.02	0.00	0.10
A1	*V*	300 m	0.25	0.63	0.82	0.05	−0.00	0.01	0.05
E2	σ_t	39 m	**0.85**	**0.95**	0.94	0.23	0.03	−0.10	0.21
E3	σ_t	120 m	0.00	**0.49**	0.45	0.25	−0.24	−0.04	0.08

[a]Model-observation statistics for mooring time series of along-shelf velocity (v) and density (σ_t). Correlations of detrended time series (CC_{DT}) significant at 95% confidence are shown in bold. Values of Willmot skill (WS) higher than that of NCOM-CCS (WS_{NCOM}) are shown in bold. Root-mean-squared error (RMSE), mean bias (MB), standard deviation error (SDE), and correlation coefficient error (CCE) are expressed in units of m s^{-1} for v, and units of kg m^{-3} for σ_t.

region of particularly complex topography, strong tides and the estuarine influence. Model skill at E3 is therefore improved over NCOM-CCS due to higher model resolution and inclusion of the strait, which is not included in the NCOM-CCS model.

At the A1 site over the British Columbia slope, improvement over NCOM-CCS is found at 35 m but not at 300 m (Figure 3 and Table 1). Modeled fluctuations are not significantly correlated with observations at

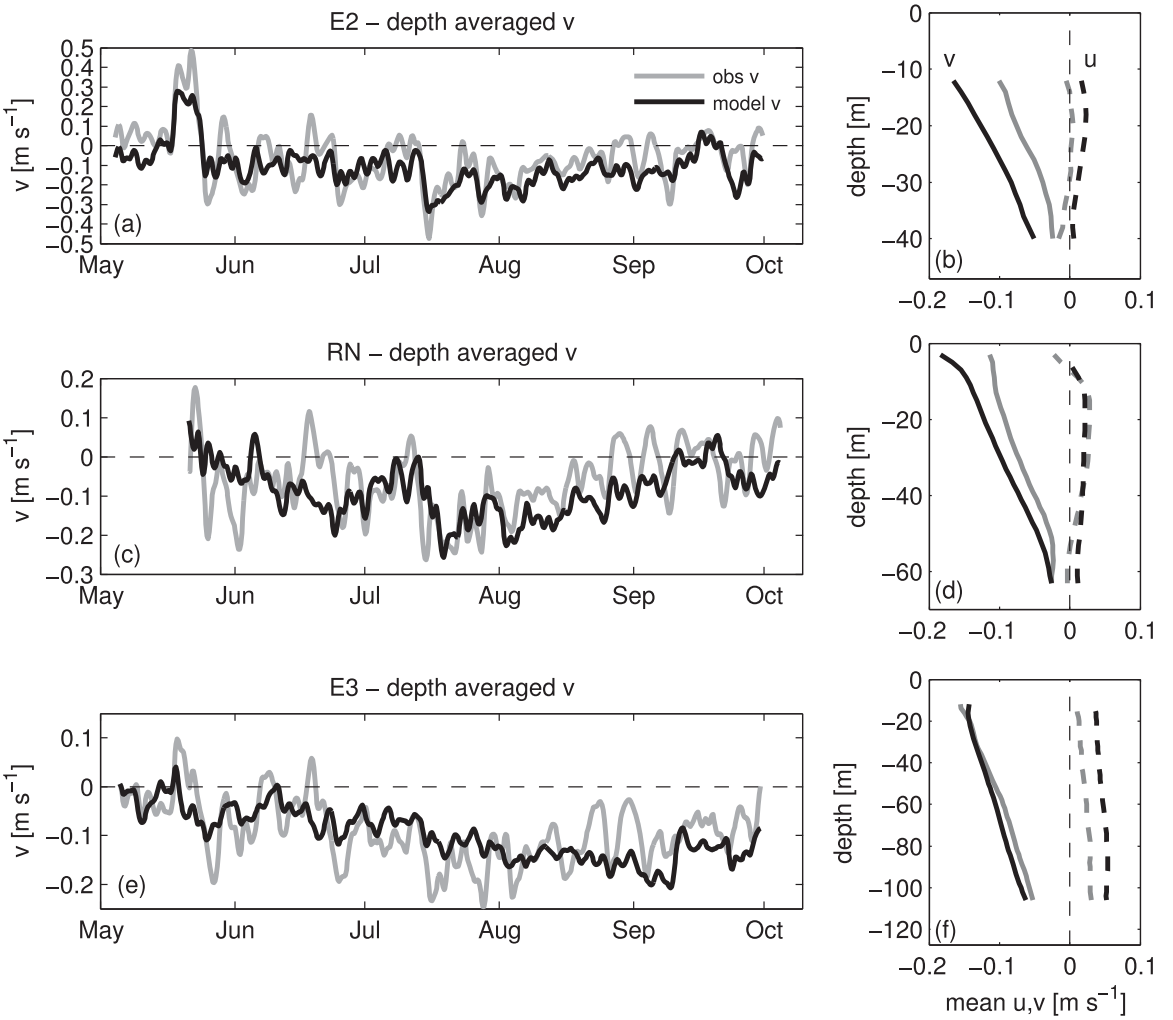

Figure 2. Modeled and observed (a, c, and e) depth-averaged velocity time series and (b, d, and f) mean velocity profiles at three mooring locations over the shelf. Thin dashed lines indicate zero velocity. Note the difference in scale between the time series.

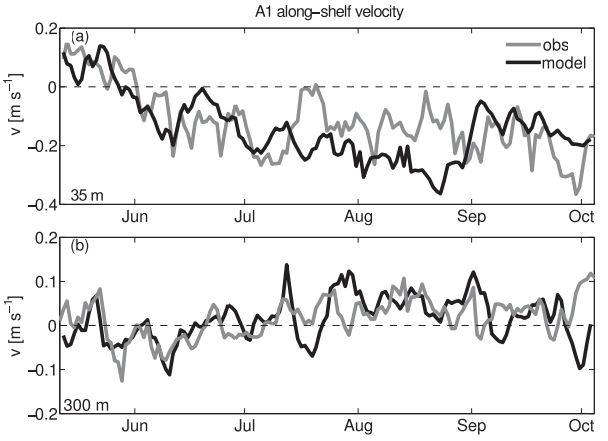

Figure 3. Modeled and observed velocity time series at the A1 mooring site over the British Columbia slope at depths (a) 35 m and (b) 300 m. Note the difference in scale.

either depth, but the model does have an equatorward shelf break jet at 35 m, and a poleward undercurrent at 300 m. The low correlation is likely related to problems incorporating remotely forced coastal trapped waves, which drive much of the variability at this location [*Connolly et al.*, 2014]. The strength of the equatorward jet is overestimated during periods in July-August (Figure 3a), but the overall mean bias is small (-0.02 m s^{-1}). The modeled flow at 300 m is equatorward during late May and early June, then becomes predominantly poleward during late July-September, similar to the observed variability over time scales of months (Figure 3b). This development of poleward flow during summer is representative of the expected seasonal cycle at this location [*Thomson and Krassovski*, 2010].

3.2.2. Near-Bottom Density

Comparisons with density time series from available near-bottom measurements at the shelf moorings are one measure of the model's representation of upwelling in the subsurface water column (Figure 4). The best agreement with observed density is found 8 m above bottom at E2, the shallowest mooring site (Figure 4a and Table 1). After a decrease in density associated with downwelling-favorable poleward flow during May (Figure 2a), which is underpredicted in the model due to the lack of a Columbia River plume, modeled and observed density increase at this location to a value of $\sigma_t \simeq 26.0$ kg m^{-3} by the end of the summer (Figure 4a). Further offshore at E3, the model shows a small improvement over NCOM-CCS (Table 1). The RMSE is dominated by the mean bias, -0.24 kg m^{-3}, which is likely due to the initial and boundary conditions from the NCOM-CCS model, which is fresher than observations by $\sim$0.2 psu [*Liu et al.*, 2009]. Both model and observations indicate a gradual trend of increasing density during June-September, $\sim$0.25 kg m^{-3} over 4 months (Figure 4c).

3.3. Shipboard Surveys

Regional shipboard surveys do not resolve individual events, but provide greater spatial coverage over the Washington shelf. The inner shelf is excluded from this analysis in order to isolate the seasonal upwelling process, rather than the higher-frequency response to local wind stress in shallower water. A bias is evident in the high salinity range but not in the corresponding low temperature range (Figure 5). The mean bias in deep salinity determined from shipboard measurements of salinity is -0.28 psu, resulting in a density bias of -0.20 kg m^{-3}, which is consistent with bottom density at the E3 mooring. Since changes in density and density gradients are most relevant for studying upwelling, this bias is not a major concern. Removing the mean bias, the RMSE calculated for the bottom water properties are 0.34°C for temperature, 0.13 psu for salinity, and 0.14 kg m^{-3} for density. These errors are $\sim$10% of the overall range present in shelf bottom water during April-September (Figure 5).

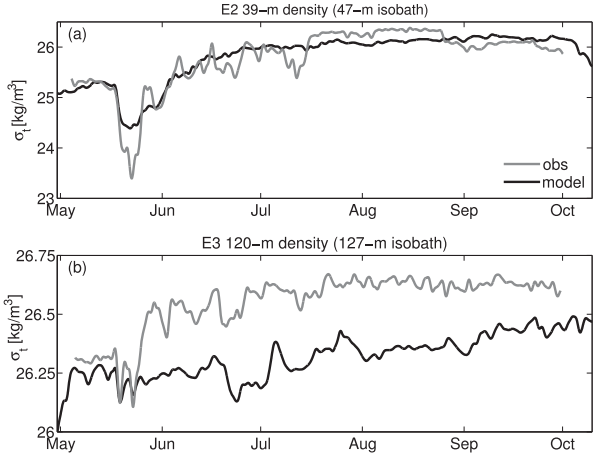

Figure 4. Modeled and observed near-bottom density time series at the (a) E2 and (b) E3 mooring sites. Note the difference in scale between the plots.

Maps of temperature at 50 m during July and September are used to compare

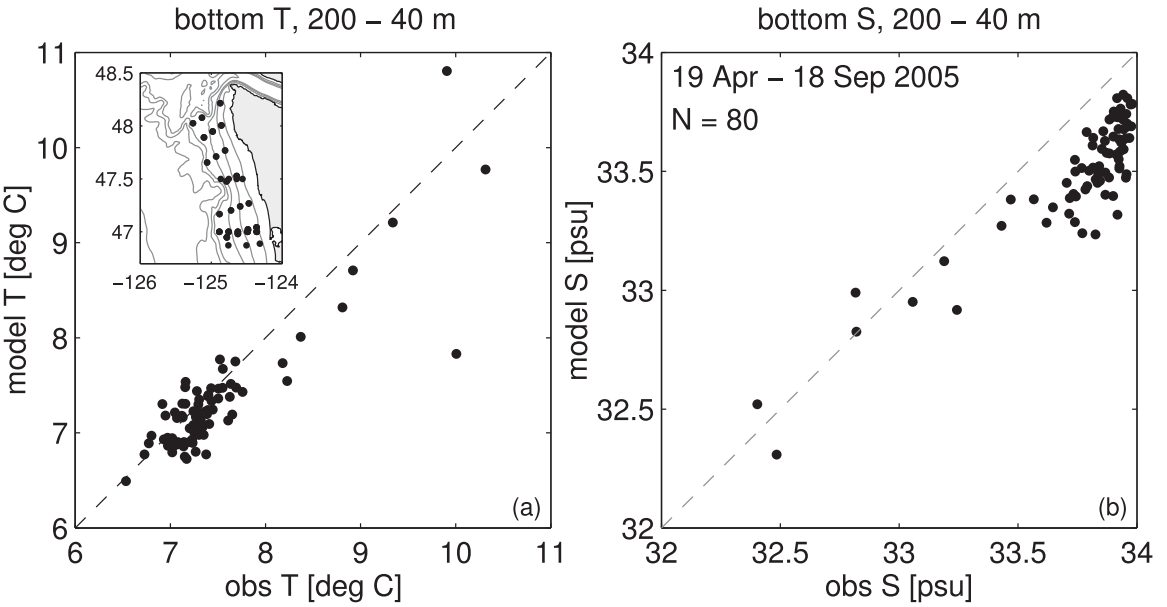

Figure 5. Comparisons of modeled and observed near-bottom (a) temperature and (b) salinity from five cruises over the Washington shelf during 19 April 2005 to 18 September 2005 ($N = 80$ samples). Locations are shown in the inset in the upper left corner of Figure 5a. Bottom depths include shallower than 40 m and deeper than 200 m are excluded in order to isolate the midshelf-upper slope region. Measurements span the time period 19 April 2005 to 18 September 2005.

regional patterns of observed and modeled seasonal upwelling (Figure 6). As noted previously, a fresh bias is present in the modeled salinity fields. During July, in both the model and observations, the coldest water (<7.5°C) is present in the Juan de Fuca eddy and directly adjacent to Cape Flattery. Outflow from the Strait of Juan de Fuca is 0.5–1°C warmer than observations, but upwelled water <8°C is found at 50 m along the Washington coast in both the model and observations. Seasonal changes between the two surveys are evident in the eddy and coastal upwelling regions. As observed, the modeled eddy core (<7.5°C) is located further offshore and has a larger horizontal extent during September. The strongest upwelling along the Washington coast is located further south during September. Offshore, temperatures are several degrees colder than observed, which may indicate an underestimate of surface heat flux and/or vertical mixing. Overall, this comparison with shipboard surveys shows that the model can be used to diagnose processes that contribute to regional patterns of upwelling over the midouter shelf and in the Juan de Fuca eddy region, as well as changes in upwelling at time scales of months.

4. Modeled Circulation in Shelf Break Canyons

Comparison with the 2005 observations in section 3 addresses the scales of regional upwelling, but not the smaller-scale canyon processes that are hypothesized to contribute to upwelling (see section 1). Although no observations are available at the smaller scales of submarine canyons during this time period, several observational canyon studies have taken place in this region. In this section, time series of modeled velocity and temperature are shown for locations where previous canyon observational studies have taken place in order to demonstrate consistency with past observations and define periods of downwelling, upwelling, and relaxation based on the incident velocity near the heads of canyons. Fields of velocity, density, and vorticity, as well as ageostrophic forces of the cross-shelf momentum balance, are used to provide a more complete view of the modeled circulation during different types of conditions at Barkley and Quinault canyons.

4.1. Barkley Canyon

Barkley canyon has width $W = 8.9$ m and indents the shelf break off British Columbia, which has depth $H_s = 200$ m. These scales, with local Coriolis frequency f and observed buoyancy frequency N [*Allen and Hickey*, 2010] correspond to a Rossby radius, $R_L = NH_s/f$, of 8.6–9.5 km and Burger number, $Bu = NH_s/fW$, of 0.97–1.07. Moored time series have previously shown evidence of cyclonic eddy formation near the depth

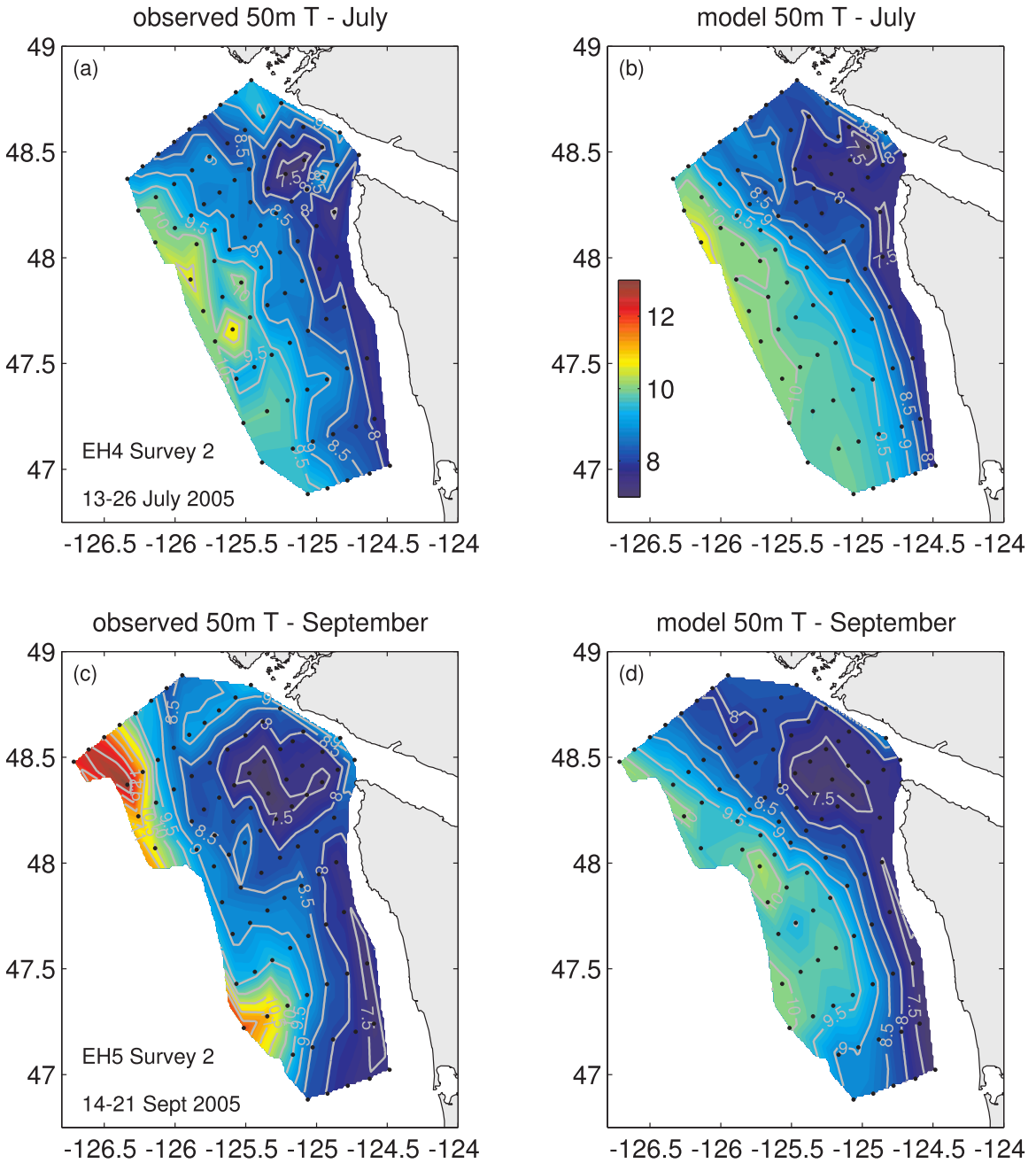

Figure 6. Maps of modeled and observed temperature at 50 m during (a and b) July and (c and d) September 2005. Model output is subsampled to the same locations and times as the observations.

of the canyon rim and have demonstrated a correlation between temperature fluctuations within the canyon and incident velocity above the canyon rim [*Allen et al.*, 2001].

Model results show that during a strong equatorward flow event at Barkley canyon, a pool of dense water, ~0.2 kg m^{-3} more dense than further offshore, is present at the head of the canyon (Figure 7a). Three days later, equatorward flow over the shelf is weaker and a cyclonic rim-depth eddy is associated with poleward flow at the canyon head at 180 m (Figures 8b and 7b). The modeled relative vorticity has a maximum of 1.2*f*. For comparison, *Allen et al.* [2001] estimated relative vorticity with magnitude 0.3*f* in Barkley canyon using a diagnostic model, and 1.7*f* by estimating stretching of isopycnals from hydrographic data (the observational estimate was considered an overestimate due to the assumption of no dissipation). The

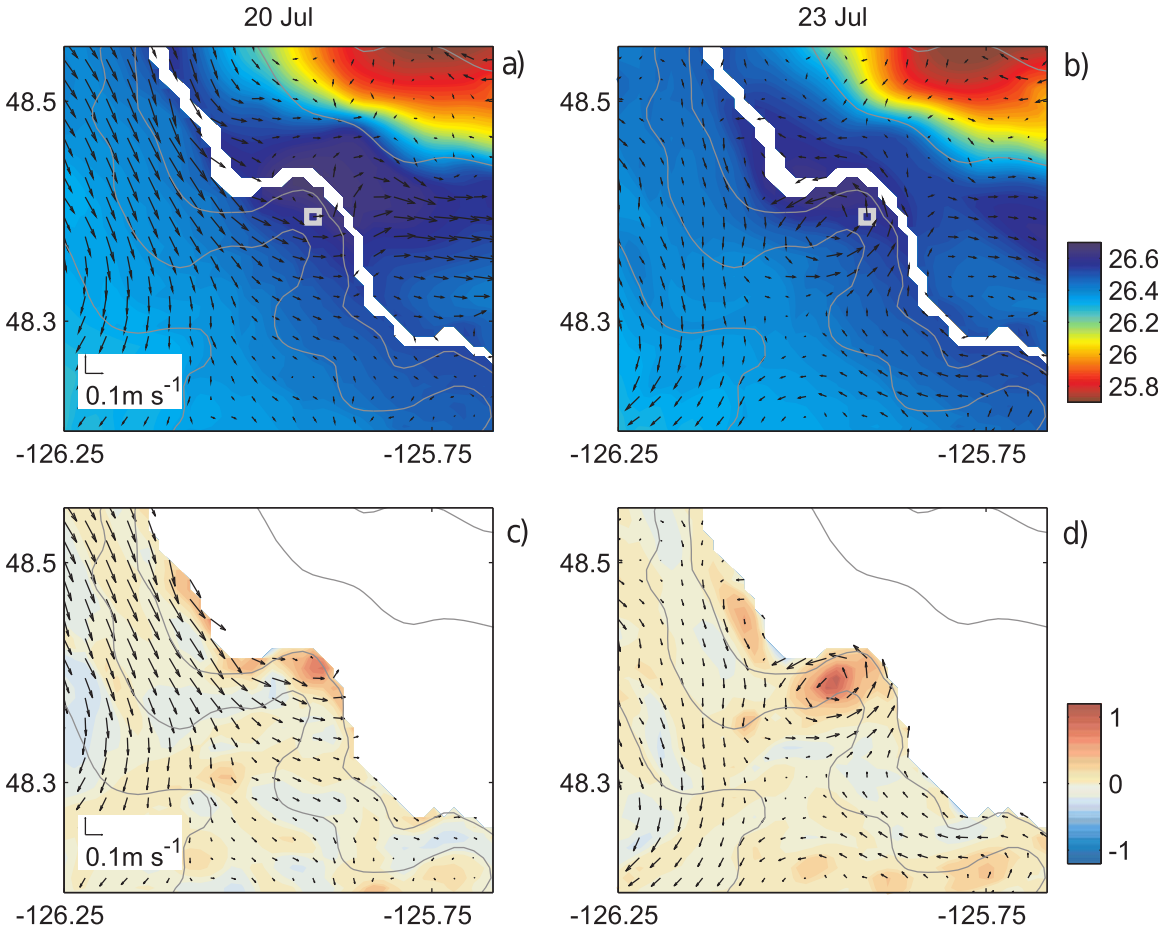

Figure 7. (a) Velocity (arrows) and density (color) near Barkley canyon on 20 July 2005, in the bottom grid cell over the shelf and at 180 m further offshore. Every other velocity vector is shown. (b) As in Figure 7a, but on 23 July. (c) Velocity (arrows) and relative vorticity (colors) at 180 m on 20 July. Vorticity is normalized by the Coriolis parameter *f*. (d) As in Figure 7c, for 23 July.

timing of eddy formation several days following the strongest equatorward flow is also consistent with the observational study of *Hickey* [1997] in Astoria canyon.

Like the observations presented by *Allen et al*. [2001], model time series from the same locations, temperature at 230 m, and along-shelf velocity at 100 m, also show a significant correlation ($R^2 = 0.51$, Figure 8a). The temperature fluctuations observed by *Allen et al*. [2001] have greater range (6–7.5°C instead of the modeled 6–6.8°C), suggesting that the model may underestimate the local upwelling response to fluctuations in the along-shelf velocity. The modeled temperature fluctuations at 230 m are not correlated with the modeled along-shelf velocity at 230 m (Figure 8b), as might be expected if the isotherms were simply adjusting to geostrophic flow at the same depth. At 230 m, along-shelf velocity is generally weak, and poleward flow events lag cold temperatures by several days. As will be seen shortly, these poleward flow events are associated with the formation of cyclonic eddies.

The observed correlation between velocity and temperature near the heads of canyons has been attributed to an ageostrophic force in the cross-shelf direction, which allows for a net flow across isobaths [*Hickey*, 1997; *Allen et al*., 2001]. In order to confirm the importance of this physical mechanism in the model, the modeled cross-shelf momentum balance is examined. The equation governing conservation of cross-shelf momentum, *u*, is

$$\underbrace{\frac{\partial u}{\partial t}}_{\text{ACCEL}} = \underbrace{-\nabla\cdot(\vec{\mathbf{u}}u)}_{\text{ADV}} \underbrace{-\frac{1}{\rho_0}\frac{\partial p}{\partial x}+fv}_{\text{AGEO}} + \underbrace{\frac{\partial}{\partial z}\left(K_M\frac{\partial u}{\partial z}\right)}_{\text{VVISC}}, \tag{4}$$

where *p* is the pressure and K_M is the eddy viscosity. The ACCEL term represents unsteady acceleration at a fixed point, ADV represents momentum advection, AGEO is the ageostrophic term obtained by summing

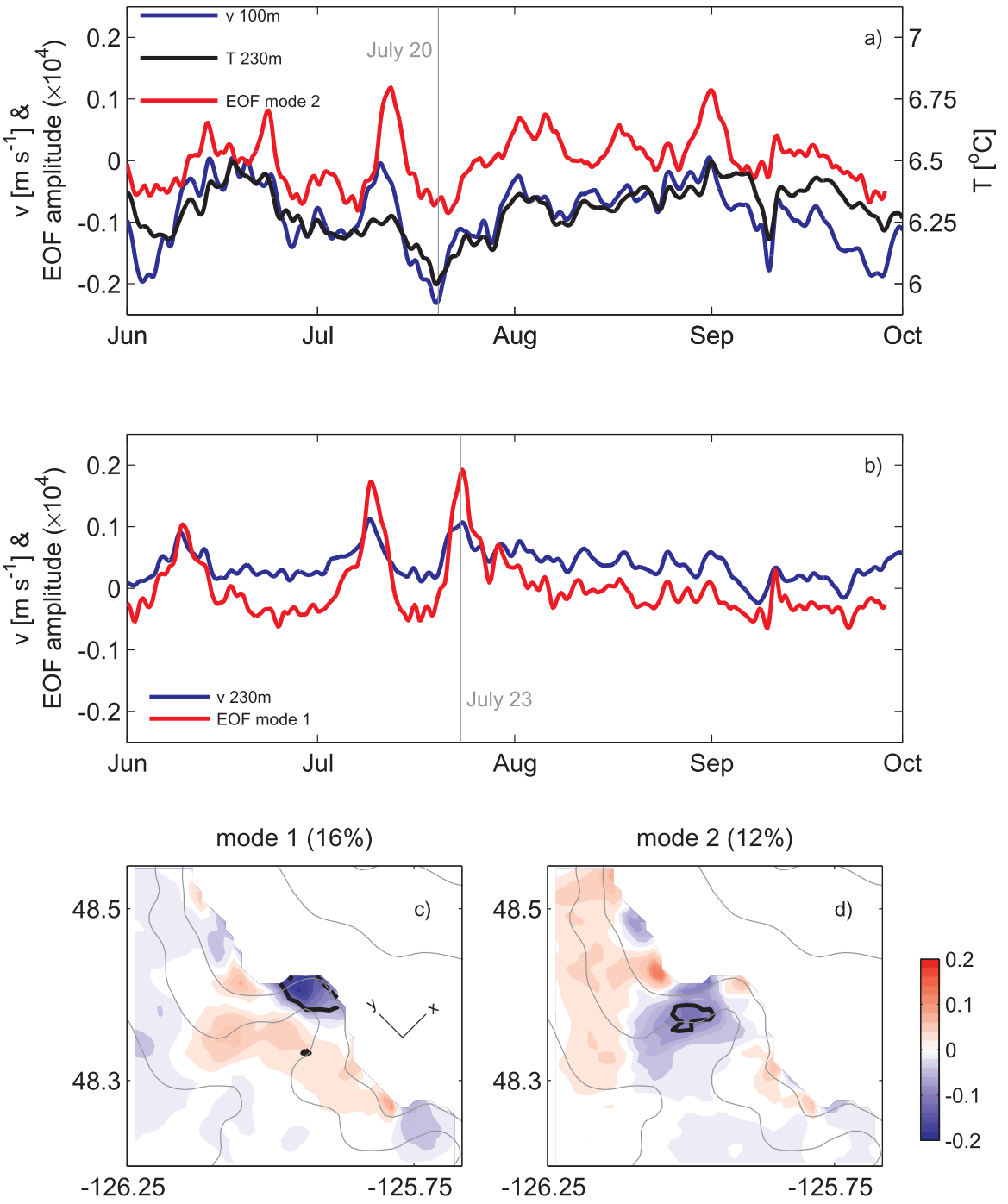

Figure 8. Velocity, temperature, and EOFs of the cross-shelf ageostrophic force near Barkley canyon. (a) Along-shelf velocity at 100 m (red, see Figure 7 for location), temperature at 230 m depth (black), and amplitude of EOF mode 2 at 180 m (blue, see Figure 8d for spatial structure). (b) Along-shelf velocity at 230 m depth (see Figure 7 for location), and amplitude of EOF mode 1 at 180 m (blue, see Figure 8c for spatial structure). Negative velocity indicates periods of equatorward geostrophic flow above the canyon. (c) Structure of the first EOF mode. Percentage indicates total variance accounted for by the EOF mode. Thick black lines enclose regions where the EOF mode accounts for >50% of the variance. (d) As in Figure 8c for the second mode.

the pressure gradient and Coriolis forces, and VVISC is the viscous force associated with vertical mixing of momentum. For an along-shelf current in geostrophic balance, the AGEO term would be equal to zero. To confirm that variability in velocity and temperature near canyons is related to ageostrophic forces in the cross-shelf direction, empirical orthogonal functions (EOFs) of the AGEO term are analyzed at 180 m near Barkley canyon. EOFs of the ADV term (not shown) are similar and of opposite sign, indicating a dynamical balance between ageostrophic forces and momentum advection.

The spatial structure of the first mode is characterized by strongest variability at the head of the canyon, near the upstream side (Figure 8c). A zero crossing is aligned perpendicular to the canyon axis, indicating that ageostrophic forces are directed toward the center of the canyon when the EOF amplitude is positive. The amplitude of the first mode shows that this structure is associated primarily with three poleward flow events at 230 m near the canyon head (Figure 8b), identified earlier as the signature of closed cyclonic eddies (e.g., Figures 7b and 7d). The structure of the EOF indicates that ageostrophic forces are directed inward toward the center of the eddy during these events. The presence of dense water near the canyon head following upwelling (Figure 7b) contributes to the offshore-directed ageostrophic force there.

The second EOF mode is characterized by strongest variability on the upstream side of the canyon (Figure 8d). This second mode is associated with an onshore ageostrophic force throughout the canyon (except for the very tip of the head) during periods when the EOF amplitude is negative. These events coincide with the appearance of equatorward flow above the canyon, which is strongest on 20 July (Figure 8a). The EOF amplitude repeatedly reverses to positive throughout August, indicating the tendency for an offshore ageostrophic force during this period when there is weak equatorward flow over the outer shelf and a strong poleward California Undercurrent over the slope (Figure 3b).

4.2. Quinault Canyon

Quinault canyon is much wider than Barkley canyon ($W = 30$ km versus 8.3 km) and indents the shelf break of Washington, which has depth 180 m. These scales and observed stratification [*Allen and Hickey*, 2010] correspond to $R_L = 12.6$ km and $Bu = 0.42$. Like Barkley canyon, upwelling has been observed in association with equatorward flow events. *Hickey* [1989] compared near-bottom along-shelf velocity and temperature at two locations over the 150 m isobath (see Figures 9a and 9b for locations). During periods of equatorward flow, colder water was observed near the head of the canyon, but not at the open slope location. Similar behavior is evident in the modeled time series at the same locations (Figure 9c). Along-shelf velocity over the open slope is not significantly correlated with temperature at the same point, but does account for 53% of the variance in temperature at the canyon head and 60% of the temperature difference between the head and open slope. In the model, temperature differences of $\sim$0.2°C occur between the two locations for 0.05 m s^{-1} equatorward flow. In the *Hickey* [1989] observations, the differences can be as large as $\sim$0.6°C for 0.10 m s^{-1} equatorward flow, indicating a possible 30% underestimate in the modeled temperature fluctuations.

At this location, the strongest upwelling in the model occurs on 16 July (Figure 9c), 4 days earlier than the strongest upwelling at Barkley canyon. Like the Barkley canyon event, cross-isobath flow is evident at the head of the canyon and relatively dense bottom water is advected to the southeast (Figure 9a). A closed cyclonic eddy is present at 180 m, but the relative vorticity ($<0.3f$, not shown) is smaller than in the Barkley canyon eddy described above due to the larger canyon width.

Two weeks later, on 31 July, relaxation from persistent upwelling-favorable wind stress is associated with much different conditions near the canyon (Figures 9b and 9d). Velocity over the shelf is close to zero and temperature is nearly identical at the open slope and canyon head locations (Figures 9b and 9c). Note that poleward flow, the California Undercurrent, is present over the slope and follows the bathymetry of Quinault canyon (Figure 9b). Poleward flow over the slope associated with the undercurrent is highly variable in time, both in the model and observations (Figure 3).

Unlike the analysis at Barkley canyon presented in section 4.1, EOFs of the ageostrophic term at Quinault canyon (not shown) are not as clearly related to canyon dynamics. Instead, movement of the anticyclonic eddy located just offshore of the canyon (Figures 9a and 9b) appears to dominate the spatial patterns of the modeled ageostrophic force in the vicinity of the canyon. However, the significant correlation identified earlier between along-shelf velocity over the outer shelf and temperature at the canyon head strongly suggests that upwelling events are associated with unbalanced cross-shelf pressure gradients near the head of canyon, as inferred previously from observations.

5. Model Experiments: Effects of Coastline and Bathymetry

In this section, the model experiments with varying coastline and bathymetry are analyzed. The impact of canyons on seasonal upwelling is determined by comparing the source depths of Lagrangian particles that

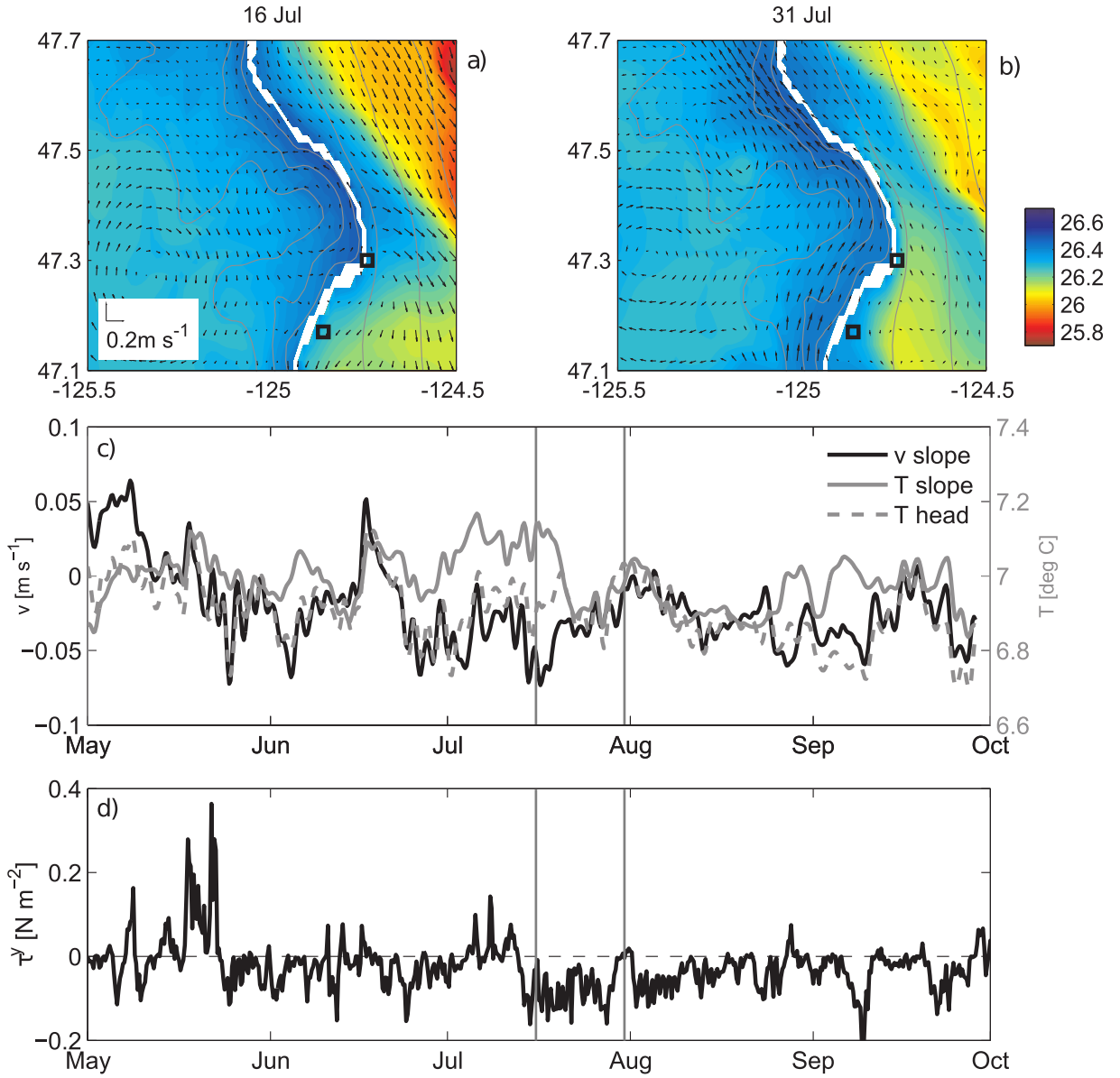

Figure 9. (a) Velocity (arrows) and density (color) near Quinault canyon on 16 July 2005, in the bottom grid cell over the shelf and at 180 m further offshore. Every other velocity vector is shown. (b) As in Figure 9a, but for 31 July. (c) Velocity and temperature over the 150 m isobath near Quinault canyon. Near-bottom along-shelf velocity over the open slope (black) and near-bottom temperature over the open slope (solid gray) and near the head (dashed gray). Times of events shown in Figures 9a and 9b are indicated by vertical gray lines. (d) Along-shelf wind stress from the model forcing over the Washington shelf (47°20.9′N, 124°42.5′W).

are upwelled onto the shelf (section 5.1) and cross-isobath fluxes over the slope in a salt budget over the shelf (section 5.2).

5.1. Source Depth

In the previous section, modeled equatorward flow events were shown to be associated with dense water at the heads of canyons and at nearby shelf locations. To further demonstrate that canyons influence the source depth of upwelled water, trajectories are tracked for Lagrangian particles that are upwelled from the slope to the midshelf of Washington. Particles are released daily throughout the water column (40–400 m, every 20 m) during April-September and tracked for 15 days (see section 2.3 for details). The 15 days time scale is used because it encompasses entire upwelling events and allows the canyon upwelling process to be fully set up [*Klinck*, 1996]. Particles transported inshore of the 100 m isobath on the midshelf are tracked,

as opposed to further offshore at the outer shelf, because these locations have greater potential to reach the euphotic zone and/or impact hypoxic events. Particle trajectories from model experiments with different coastlines and bathymetry (see section 2.2 for details) are also analyzed in order to provide further evidence for the effects of bathymetry on source depth.

In the primary realistic model run, the deepest source depths (140–260 m) for particles advected from the slope to the Washington midshelf are associated with particles that originate near Quinault canyon and the mouth of Juan de Fuca canyon (Figure 10a). Particles with relatively deep source depths (140–180 m) also

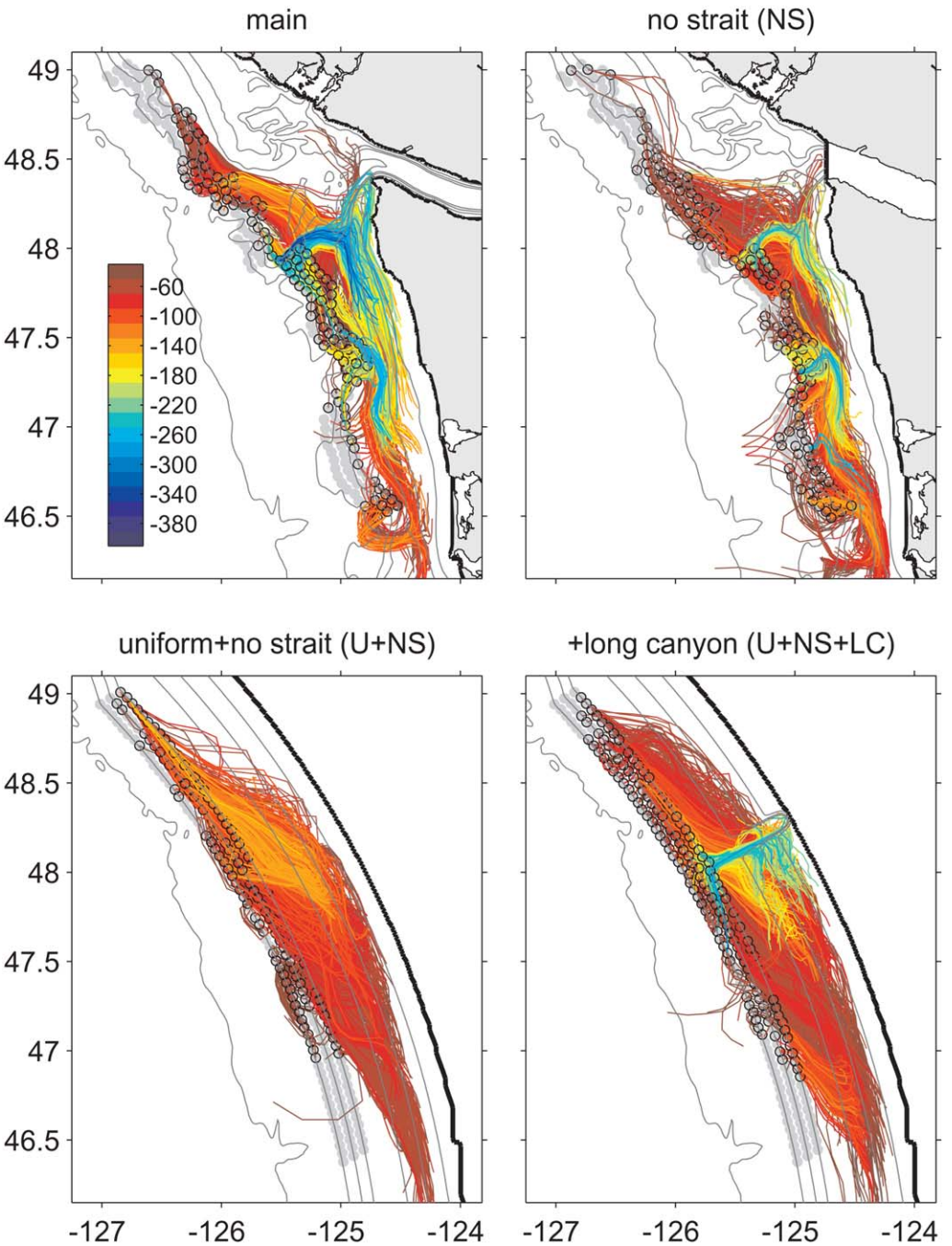

Figure 10. Trajectories of passive particles released during April-September over the slope (at locations indicated by gray circles) that pass within the 100 m isobath over the Washington shelf within 15 days, colored by source depth at the starting point over the slope (black open circles). Trajectories with the deepest source depths are plotted on top. (a) Main model run, (b) no Strait of Juan de Fuca (NS), (c) uniform shelf and no strait (U + NS), (d) uniform shelf with no strait, plus a long canyon (U + NS + LC).

originate near Barkley canyon, located further north on the British Columbia shelf. A histogram of source depths for all the mapped trajectories shows a broad peak centered near the shelf break at 120–180 m, superimposed on a decrease in the number of particles with depth (Figure 11a). At the end of the 15 days trajectories, upwelled particles are concentrated near the bottom (Figure 11b). Twenty-eight percent of the upwelled particles are found within 10 m of the bottom, and the number of upwelled particles decreases with height above the bottom.

Since it is possible that the upwelling through Juan de Fuca canyon could be influenced by the sharp coastline curvature at Cape Flattery and estuarine outflow from the Strait of Juan de Fuca, particles were also tracked for an identical run with a closed boundary at the entrance of the strait ("NS," Figure 10b). Outflow from the strait is dynamically significant because the volume flux ($\sim 10^5$ m^3 s^{-1}) [*Thomson et al.*, 2007] is approximately equal to the Ekman transport associated with 0.1 N m^{-2} wind stress along 100 km of coastline at this latitude. Differences in mean alongshore velocity between the main run and NS run during June-September highlight the poleward flow over the BC shelf associated with buoyant outflow from the strait, and also show that stronger equatorward flow occurs over most of the Washington shelf when the strait is present (Figure 12). The largest differences in equatorward flow are located on the offshore side of the Juan de Fuca eddy and near Cape Flattery.

Without the strait, locations of deep upwelling near canyons are similar to the main model run, but no deep particles are upwelled directly adjacent to Cape Flattery (Figure 10b). The histogram of source depths indicates that the broad peak at 120–180 m is eliminated in the NS run (Figure 11a), which is likely associated with decreased equatorward flow on the outer shelf upstream of Juan de Fuca and Quinault canyons. Despite these differences when the strait is not present, canyon enhancement of upwelling is still evident in the trajectories of the deepest upwelled water (Figure 10b), and source depths are still found to be as

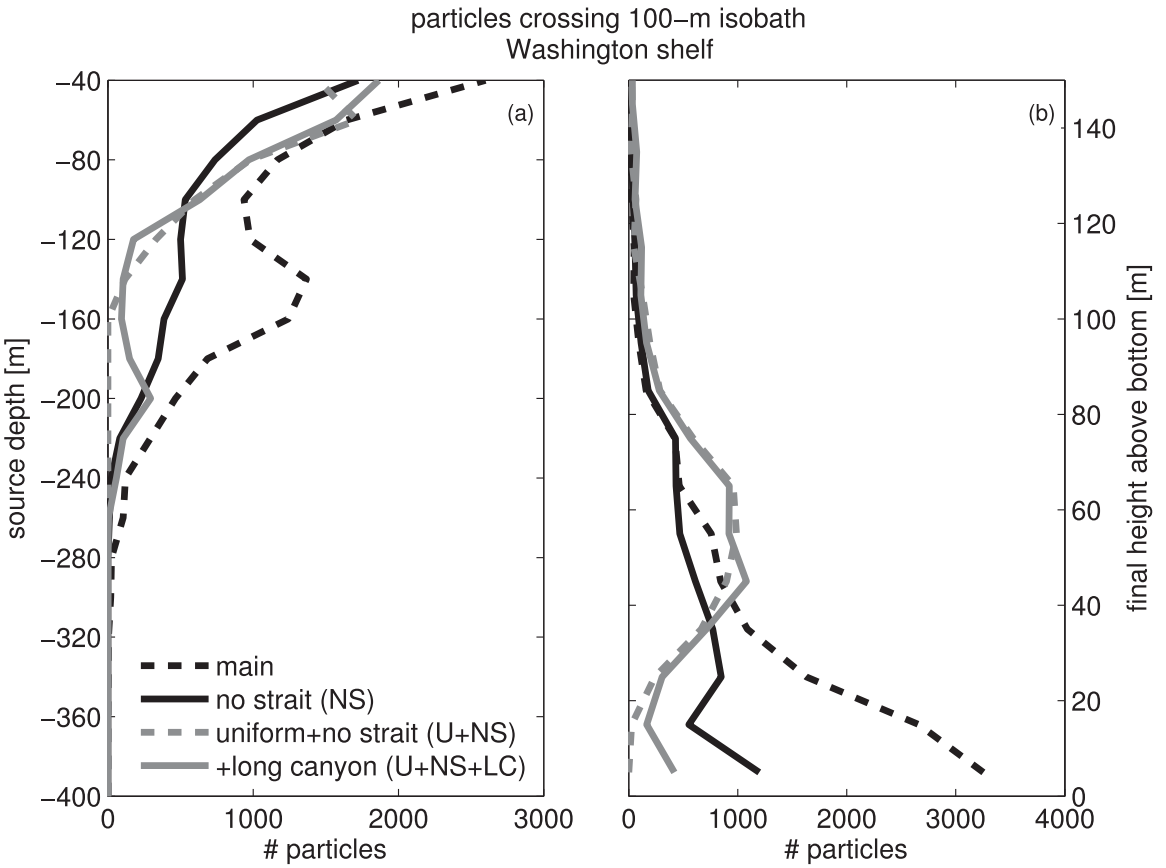

Figure 11. (a) Histograms of source depths for all trajectories shown in Figure 10. Particles were released every 20 m between 40 and 400 m at locations over the slope. (b) Histograms of the final height above bottom for the same particles, in 10 m bins.

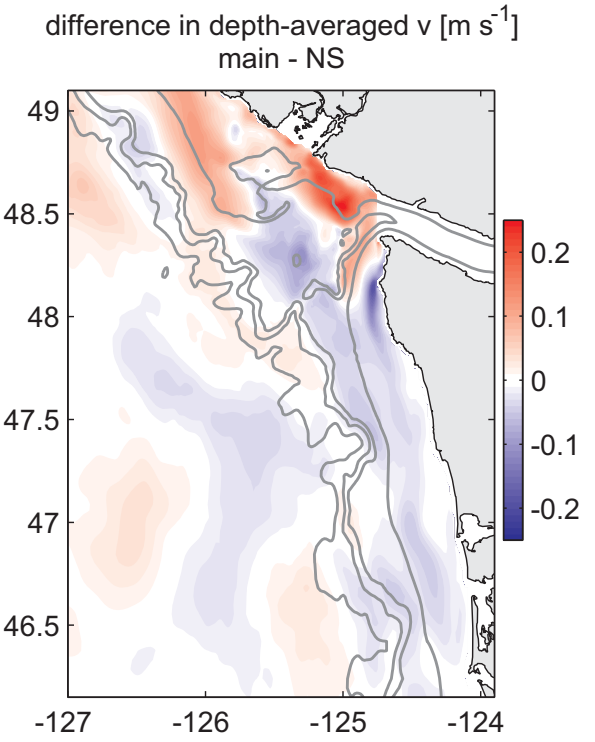

Figure 12. Difference in depth-averaged along-shelf velocity, *v*, between the main run and no strait (NS) run, averaged over the period June-September. Red and blue indicate stronger poleward and equatorward velocity, respectively, in the main run. The along-shelf direction is defined by the radial coordinate system described in section 2.2.

deep as 240 m (Figure 11a). As with the main run, the greatest number of upwelled particles over the shelf is found near the bottom after 15 days (Figure 11b).

For comparison to a case without canyons, the model was also run with the same forcing and boundary conditions, but with modified bathymetry that is uniform in the along-shelf direction and has no strait ("U + NS," Figure 10c). In this case, there is a large-scale gradient with deeper source depths to the south, but source depths never exceed 150 m (Figure 11a). At the end of the 15 day trajectories, the majority of particles are located 40–70 m above the bottom and none are found in the bottom 10 m (Figure 11b). In the U + NS case, onshore movement of water from the slope to midshelf is restricted, source depths for upwelling from the slope to shelf are relatively shallow, and upwelled particles end up in the interior water column rather than the bottom 10 m.

In the final model run, a canyon with geometry resembling Juan de Fuca canyon is added to the uniform shelf with no strait in order to isolate the effect of this canyon from the other complex bathymetric features of the region ("U + NS + LC," Figure 10d). In this case, source depths deeper than 150 m are present, and a secondary peak in source depth occurs at 200 m (Figure 11a). Upwelled particles associated with this enhancement are found near the bottom (Figure 11b). This long canyon geometry not only provides deep source depths, but also brings particles that have been upwelled from the slope close to the inner shelf (Figure 10d).

5.2. Salt Budget

The previous section showed that submarine canyons influence the source depth of upwelled water, allowing for upwelling of water from deeper than 150 m to midshelf. In order to quantitatively relate this enhancement of upwelling to the seasonal changes in tracers over the shelf, budgets are computed in each of the model runs with varying bathymetry for a conservative tracer (salt). An isohaline coordinate system is used to compare the salinity values at which the onshore flux of water occurs in each model run, as well as the cumulative seasonal changes in volume-integrated salt content over the shelf.

5.2.1. Formulation

The salt budget is formulated in isohaline coordinates rather than fixed-depth (*z*-level) coordinates. This method of decomposing the budget, recently summarized by *MacCready* [2011] in the context of estuarine exchange flow, can be used to quantify the salinity values at which the cross-shelf fluxes of water associated with upwelling occur. In comparing model runs, upwelling from greater depths is associated with onshore fluxes at higher salinities.

The balance between changes of volume-integrated salinity and fluxes of salt across the boundaries can be expressed in isohaline coordinates as

$$\frac{d}{dt}\int SdV = \int S\frac{\partial Q}{\partial S}dS, \tag{5}$$

where S is salinity, V is the shelf volume, and

$$Q(S') = \int_0^{S'} \frac{\partial Q}{\partial S}dS, \tag{6}$$

is the volume flux across the boundaries at salinity values less than or equal to S'. In the present context of shelf-slope exchange, if an onshore flux of high-salinity water occurs near a submarine canyon, and an equal but opposite offshore transport of lower-salinity water occurs at the same depth further downstream, onshore volume flux is recorded at the higher salinity class rather than a net sum of zero at a fixed depth.

To obtain $\partial Q/\partial S$ from model results, velocities normal to the shelf volume are binned into discrete salinity classes ($\Delta S = 0.05$ psu), integrated over the cross-sectional area of the grid cells, and normalized by ΔS. Analysis is focused on the Washington shelf volume shown in Figure 1, from land to the 100 m isobath on the offshore edge, consistent with the analysis of Lagrangian particles in section 5.1. Total volume varies by $<3\%$ between model runs.

5.2.2. Cumulative Increase in Salinity Associated With Seasonal Upwelling

The model runs with variable bathymetry can be used to test whether the presence of submarine canyons is associated with a higher cumulative increase in salinity over the shelf during the summer upwelling season. In order to isolate the effect of modifying the bathymetry, only the three model runs with no Strait of Juan de Fuca are compared. Fresh outflow associated with estuarine circulation in the Strait of Juan de Fuca significantly decreases volume-averaged salinity over the Washington shelf (not shown). It is found that the NS run, which retains the complex bathymetry of the main model run with no fresh water source from the strait, experiences the highest cumulative increase in salinity over the shelf during the early part of the summer season (Figure 13). During the period 1 June-25 July, the volume-averaged salinity in this run exceeds that of the uniform bathymetry case (U + NS) by 0.1–0.2 psu. Smaller differences ($\leq$0.1 psu) are found between the U + NS case and the long-canyon (U + NS + LC) case, but salinity is usually slightly higher with the long canyon included. Although the effect of a single long canyon on volume-averaged salinity is relatively small, it will shown later that the long canyon has a much greater effect on near-bottom salinity over the inner shelf.

Later in the summer, during August and September, volume-averaged salinity is more similar between model runs (Figure 13). During August, volume-averaged salinity in the NS run falls ~0.05 psu below that of the runs with simplified bathymetry. The small difference in volume-averaged salinity between the NS and U + NS runs during this part of the season indicates a lack of canyon-enhanced upwelling. This period is associated with weak equatorward currents on the outer shelf and the presence of the poleward California Undercurrent over the slope (see Figures 9b and 9c). However, when equatorward flow on the outer shelf reappears during late August and early September, salinity increases most rapidly in the NS run with complex bathymetry (Figure 13).

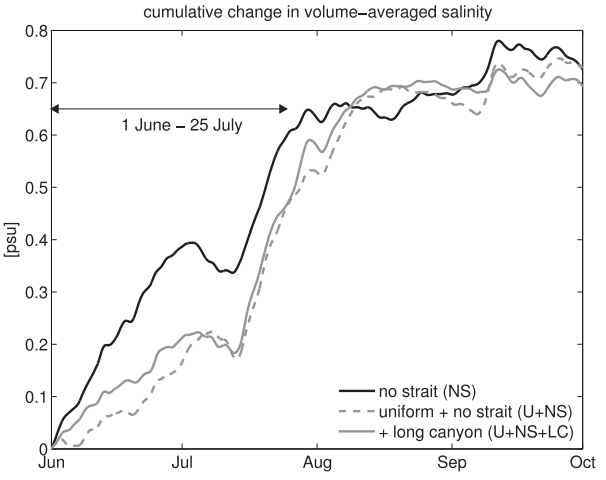

Figure 13. Cumulative change in volume-averaged salinity in the Washington shelf control volume shown in Figure 1. Three different model runs with different bathymetry are compared: no Strait of Juan de Fuca (NS, solid black), uniform shelf with no strait (U + NS, dashed gray), and uniform shelf with no strait (U + NS + LC).

The enhancement of upwelling associated with submarine canyons is not

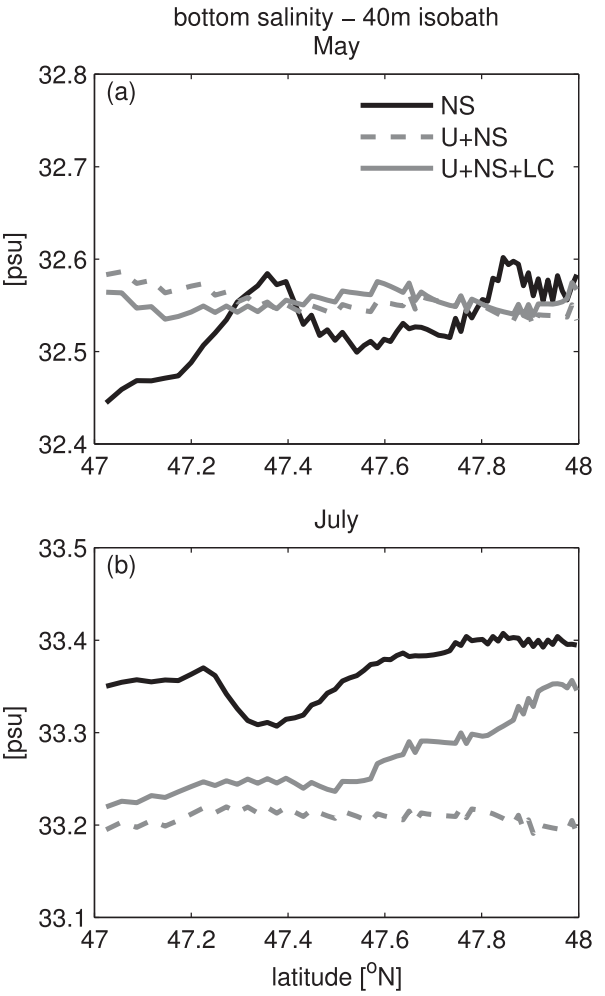

Figure 14. Spatial variations of near-bottom salinity at the 40 m isobath, averaged over the months of (a) May and (b) July. Three different model runs with different bathymetry are compared, as in Figure 13. Note that salinity values on the *y* axis are higher during July in Figure 14a, but the range of salinity values are the same in both plots.

uniformly distributed over the shelf and cannot have a great impact on coastal productivity if the upwelled water does not reach the inner shelf, where upwelling of nutrient-rich water into the euphotic zone occurs. To determine whether differences in salinity between the model runs extend to the edge of the inner shelf, near-bottom salinity values along the 40 m isobath are compared in the three runs with different bathymetry but no strait. During May, preceding the strongest seasonal upwelling, the average near-bottom salinity over the 40 m isobath is similar between the two runs with simplified bathymetry (U + NS, U + NS + LC, Figure 14a). There is little variation with latitude in either of these two runs during May. The NS run shows similar background values of salinity, but greater along-shelf variability during May, which at the shallow 40 m isobath could be associated with bends in the coastline. During July, when seasonal upwelling is strongest, greater differences of up to 0.2 psu occur between the model runs (Figure 14b). With a uniform shelf, there is little along-shelf variation. When a long canyon intersects the uniform shelf, salinity is elevated by up to 0.15 psu toward the north. This pattern suggests that the increase in salinity from 47.4°N to 48°N in the NS case is associated with the presence of Juan de Fuca canyon. Therefore, although the influence of a single long canyon on volume-averaged salinity is relatively small, it has greater effect on near-bottom salinity over the inner shelf near the coast.

5.2.3. Salinity Classes of Onshore Transport Associated With Seasonal Upwelling

To show that differences in salinity between model runs are associated with a shift to higher salinity classes in the onshore flow, mean profiles of $\partial Q/\partial S$ from different model runs are compared (Figure 15). The profiles are averaged over the period 1 June-25 July, when differences in volume-averaged salinity between runs are greatest (Figure 13). Volume fluxes across the offshore edge of the control volume (Figure 15a) are directed onshore at higher salinity classes and offshore at lower salinity classes, consistent with the presence of a seasonal upwelling circulation. Fresh water associated with the Strait of Juan de Fuca is evident in the main run as net flow into the shelf volume at low salinities (Figure 15b) and lower-salinity flow away from the coast at the offshore edge (Figure 15a). Net inflow at low salinity classes in runs with no strait (31.5–32.2 psu, Figure 15b) is associated with a large-scale salinity gradient of relatively fresh water to the north.

To highlight differences between model runs at the highest salinity classes, where submarine canyons are expected to have the greatest influence, the profiles of $\partial Q/\partial S$ are presented over the range 33.0–33.8 psu for all model runs (Figures 15c and 15d). The model runs with realistic bathymetry (main, NS) have two local

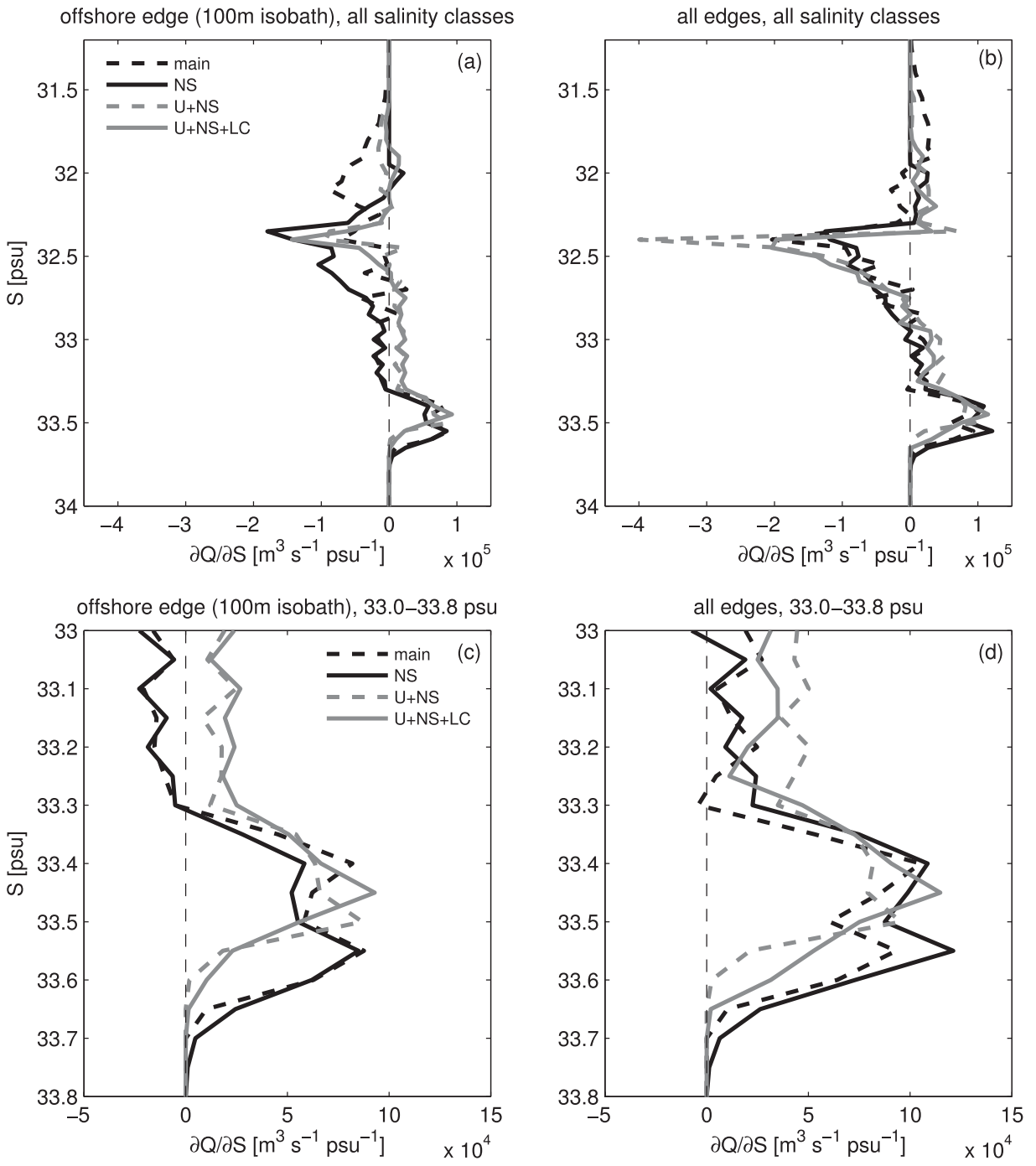

Figure 15. Volume fluxes through salinity classes, $\partial Q/\partial S$, during 1 June to 25 July at edges of the Washington shelf control volume shown in Figure 1. (a) Western edge only, (b) sum of all edges (northern, western, and southern). (c and d) As in plots 15a and 15b, but deep salinity classes 33.0–33.8 psu only.

maxima in the mean $\partial Q/\partial S$ profiles (Figure 15c). At the highest salinity classes ($S > 33.5$ psu), these runs are characterized by greater volume flux across the 100 m isobath than the runs with simplified bathymetry, which only have one local maximum in the $\partial Q/\partial S$ profile. At lower salinity classes, $S < 33.3$ psu, there is weak offshore flow in the runs with realistic bathymetry and weak onshore flow in the runs with simplified bathymetry.

When all edges of the volume are considered, the flux of higher-salinity water is also enhanced in the run with a long canyon (U + NS + LC) compared with U + NS run (Figure 15d), demonstrating the influence of Juan de Fuca canyon north of the Washington shelf. In the run with uniform bathymetry, no significant net

transport into the Washington shelf control volume occurs at $S > 33.6$ psu (Figure 15d). Further offshore over the 250 m isobath, where Lagrangian particles originated (see section 5.1), the 33.6 psu isohaline rests at an average depth of 150 m during this time period (not shown). Therefore, analysis of isohaline salt budget and Lagrangian particles both lead to the conclusion that upwelling from depths greater than 150 m along the Washington shelf only occurs with complex bathymetry that includes submarine canyons.

6. Impact on Nutrients and Dissolved Oxygen

High-salinity water that originates from greater depths over the continental slope is characterized by relatively high concentrations of nitrate (NO_3^-), which contribute to primary productivity, and low concentrations of dissolved oxygen (O_2), which contribute to hypoxia [*Landry et al*., 1989; *Connolly et al*., 2010]. Using relationships between salinity, nitrate, and oxygen, results from the salt budget presented above can be extended to provide a quantitative estimate of the impact of submarine canyons on concentrations of nitrate and dissolved oxygen in the near-bottom water over the continental shelf of Washington.

During the June-July portion of the upwelling season, the average incoming salinity near the bottom is higher in the presence of submarine canyons (Figure 15), which is associated with a 0.1–0.2 psu difference in the cumulative increase in salinity compared to the case with uniform bathymetry (Figures 13 and 14). The regression between nitrate and salinity has a slope of 9.59 μM/psu in the $S = 33 - 33.8$ psu range (K. Davis, UC Irvine, personal communications, 2013). Using this relationship, a 0.1–0.2 psu difference in volume-averaged salinity between model runs would correspond to a 1–2 μM difference in volume-averaged nitrate. Integrating this estimate over the entire 2.0×10^{11} m^3 control volume used in the salt budget gives a total input of $\sim 1\text{–}2 \times 10^7$ kg NO_3^- during the 2 month June-July period.

This model-derived estimate of nitrate input due to canyon enhancement can be compared with a previous estimate by *Hickey and Banas* [2008]. Using typical values of the observed cross-shelf velocity associated with canyon upwelling, thickness of the upwelling layer and nitrate concentrations over the slope, *Hickey and Banas* [2008] estimated a $2\text{–}5 \times 10^8$ kg NO_3^- input due to canyon enhancement between latitudes 46°N and 50°N during spring (April-June). Scaling this estimate to be over 2 months duration and 1° latitude gives an input of $3\text{–}8 \times 10^7$ kg NO_3^-, 3–4 times larger than the model-derived estimate of $1\text{–}2 \times 10^7$ kg NO_3^-, but within the same order of magnitude. The shorter 2 month duration of the early part of the summer upwelling season in the model analysis accounts for the late spring transition documented during 2005 [*Hickey et al*., 2006; *Kosro et al*., 2006]. During late summer, there is less difference in volume-averaged salinity between model runs with different bathymetry (Figure 13), consistent with the assumption made by *Hickey and Banas* [2008] that canyon enhancement stops after the seasonal development of the California Undercurrent during late summer. The model results are subject to error and likely underestimate canyon enhancement since temperature fluctuations are reduced by up to a factor of two compared with previous observations (section 4.1). Thus, the results are consistent with the hypothesis that canyon enhancement provides a significant fraction of the nitrate that is eventually upwelled to the euphotic zone at the inner shelf by local upwelling-favorable winds.

The impact of canyon-enhanced upwelling on regional hypoxia can be estimated in a similar manner. *Connolly et al*. [2010] show that concentrations over the Washington slope have a consistent relationship with salinity, and vary inversely with nitrate concentrations at a slope of ~10 mol O_2/mol NO_3^-. A 0.1–0.2 psu difference in salinity and 1–2 μM difference in nitrate associated with the presence of submarine canyons therefore corresponds to difference in O_2 concentrations of ~10–20 μM, or ~0.2–0.4 mL/L. A difference of this magnitude is ecologically significant considering the difference between normal levels of hypoxia that are often observed on the Washington coast (~1.4 mL/L) and "severe hypoxia" associated with mortality of marine organisms (~0.5 mL/L). On the Washington coast, observational analysis has shown that biological processes contribute significantly to the seasonal reduction of O_2 during late summer [*Connolly et al*., 2010]. The lack of significant canyon enhancement during late summer, <0.1 psu difference in salinity when canyons are present (Figures 13 and 14), likely favors biological reduction of O_2 by reducing the flushing of shelf bottom water that is exposed to respiration.

7. Discussion and Conclusions

1. *Submarine canyons are associated with deeper sources of water upwelled from the slope to midshelf compared with uniform slope bathymetry*. In contrast to other slope locations, and a model run with bathymetry

that is uniform in the along-shelf direction, canyons allow for upwelling from source depths >150 m. Source depths for midshelf water in the primary realistic model run occur as deep as 260 m and show a peak bracketing 150 m (section 5.1), which is approximately the depth of the canyon heads (130–170 m) [*Allen and Hickey*, 2010]. This deep source of upwelled water increases the salinity of onshore flow from the slope to midshelf during the early part of the upwelling season, which increases the volume-averaged salinity over the shelf (section 5.2). Nitrate input estimated from these model results is consistent with the canyon enhancement estimated by *Hickey and Banas* [2008] within a half order of magnitude (section 6), a significant fraction of the nitrate upwelled to the euphotic zone by local alongshore wind stress. The onshore flux of deep water associated with submarine canyons increases average salinity by ~0.1–0.2 psu on over the midouter shelf during early summer, suggesting an important regional-scale influence on nitrate (~1–2 μM) and dissolved oxygen (~0.2–0.4 mL/L) during this part of the upwelling season. Canyon enhancement during early summer likely results in earlier onset of hypoxia and prolonged exposure of bottom-dwelling organisms to low-oxygen conditions.

2. *Canyon enhancement of upwelling influences the properties of near-bottom water over the midshelf and inner shelf*. Submarine canyons not only influence the source depth of upwelling from the slope, but also the subsequent height above the bottom for water over midshelf. When bathymetry is uniform in the along-shelf direction, particles upwelled from the slope generally reach a shallow final position in the midshelf water column after 15 days, ~50 m above bottom on average and zero particles within 10 m above the bottom (section 5.1). When submarine canyons are present, particles are upwelled to positions much closer to the bottom over midshelf (28% within 10 m from the bottom). Compared with uniform bathymetry, upwelling near canyons has a more direct influence on near-bottom water over the shelf.

The presence of canyons increases the salinity of near-bottom water at the edge of the inner shelf. When canyons are present, bottom salinity at the 40 m isobath is 0.1–0.2 psu higher during summer than the case when bathymetry is uniform in the alongshore direction (section 5.2.2). The time scale for water to reach the inner shelf from the slope is longer than the 15 days period used for particle tracking, and it is likely that much of the water upwelled through shelf break canyons is advected further south. In a Lagrangian study of upwelling during the same year off Oregon, *Rivas and Samelson* [2011] found that relatively few particles upwelled to the inner shelf over the course of 6 months trajectories originated over the slope compared with their northern boundary at 48°N. Thus, canyon upwelling off northern Washington and British Columbia likely influences the properties of inner-shelf bottom water to the south. In the present study, Juan de Fuca canyon likely has the greatest influence on the Washington inner shelf because it extends all the way to the coast, as discussed further below.

3. *A long canyon that extends to the coast (Juan de Fuca) facilitates upwelling from greater depths and to locations closer to the coast than shelf break canyons*. The present study demonstrates the particular regional importance of Juan de Fuca canyon, a long canyon that cuts through the shelf and extends into a large estuary. Particles upwell close to the inner shelf within 15 days, much closer to shore than particles that upwell through the shelf break canyons (section 5.1.). The presence of an isolated, long, 10 km wide canyon that extends to the coast, similar to the geometry of Juan de Fuca canyon, results in a deep local maximum in source depth at 200 m, deeper than results from the shelf break canyons. In addition, this canyon strongly influences bottom salinity at the edge of the inner shelf (section 5.2.2). Juan de Fuca canyon is also unique because it provides a conduit for the exchange flow of the Salish Sea [*Sutherland et al*., 2011]. Vertical mixing in the Strait of Juan de Fuca provides a separate mechanism for deep nutrient-rich water to reach the euphotic zone over the Washington shelf [*Hickey and Banas*, 2008].

4. *Upwelling events and cyclonic eddy formation at shelf break canyons are dynamically associated with variability in regional-scale along-shelf currents at the outer shelf*. The dynamics of canyon upwelling in the regional model presented here are consistent with previous studies, demonstrating that a shoreward ageostrophic force occurs near the canyon mouth during periods of equatorward flow at the outer shelf (section 4.). Upwelling of dense water at the canyon head can weaken the onshore component of the pressure-gradient force associated with the equatorward jet, consistent with the model study of *She and Klinck* [2000]. The presence of dense water at the canyon head contributes to the ageostrophic force that is directed inward toward the center of the canyon and is associated with strong cyclonic vorticity following the equatorward flow events.

Unlike previous canyon studies, the model results presented herein have retained important regional features such as the poleward California Undercurrent. Because the pressure-gradient force associated with poleward flow is directed offshore, it is often assumed that the development of the California Undercurrent shuts down canyon upwelling in the northern CCS after June [*Hickey and Banas*, 2008]. The model in the present study has an undercurrent that develops after June, consistent with observations over the British Columbia slope (section 3). The strongest modeled canyon upwelling events occur during mid-July when the undercurrent is relaxed in both the model and observations. Since event-scale variability over the slope is largely driven by first-mode coastal trapped waves [*Connolly et al*., 2014], poleward flow in the undercurrent often relaxes or reverses when shelf flow is strongly equatorward. Therefore, the presence of event-scale variability over the slope means that canyon-enhanced upwelling of slope water from below the shelf break to the midshelf can still occur during late summer, but less frequently than during the earlier part of the summer. The effect of poleward undercurrents on shelf break canyons and the dynamics of long canyons that extend to the coast are two subjects which would benefit in the future from high-resolution observational arrays set within a regional observing system, and coordinated modeling at multiple scales.

Acknowledgments

This research would not have been possible without the help of Parker MacCready, Neil Banas, and other members of the UW coastal modeling group who contributed modeling resources and valuable insight. The authors also thank Richard Thomson (IOS) for providing A1 mooring data, Edward Dever (OSU) for providing RN mooring data, Igor Shulman for providing NCOM model output, Michael Foreman (IOS) for providing tidal model output, and Cliff Mass (UW) for providing MM5 atmospheric model output. Two anonymous reviewers contributed useful and constructive suggestions on an earlier version of the manuscript. This work was part of T. Connolly's graduate research at University of Washington and was supported by grants from the Coastal Ocean Program of the National Oceanic and Atmospheric Administration (NOAA) (NA17OP2789, NA09NOS4780180) and the National Science Foundation (NSF) (OCE0234587, OCE0942675) as part of the ECOHAB PNW and PNWTOX projects. This is ECOHAB contribution 788, ECOHAB PNW contribution 34, and ECOHAB PNWTOX contribution 9. The statements, findings, conclusions, and recommendations are those of the participants/authors and do not reflect the views of NSF, NOAA, or the Department of Commerce.

References

Allen, S., C. Vindeirinho, R. Thomson, M. Foreman, and D. Mackas (2001), Physical and biological processes over a submarine canyon during an upwelling event, *Can. J. Fish. Aquat. Sci.*, *58*, 671–684.

Allen, S. E. (1996), Topographically generated, subintertial flow within a finite length canyon, *J. Phys. Oceanogr.*, *26*, 1608–1632.

Allen, S. E. (2000), On subinertial flow in submarine canyons: Effect of geometry, *J. Geophys. Res.*, *105*(C1), 1285–1297.

Allen, S. E., and B. M. Hickey (2010), Dynamics of advection-driven upwelling over a shelf break submarine canyon, *J. Geophys. Res.*, *115*, C08018, doi:10.1029/2009JC005731.

Battisti, D. S., and B. M. Hickey (1984), Application of remote wind-forced coastal trapped wave theory to the Oregon and Washington coasts, *J. Phys. Oceanogr.*, *14*, 887–903.

Beckmann, A., and D. B. Haidvogel (1993), Numerical simulation of flow around a tall isolated seamount. Part I: Problem formulation and model accuracy, *J. Phys. Oceanogr.*, *23*, 1736–1753.

Boyer, D. L., X. Zhang, and N. Pérenne (2000), Laboratory observations of rotating, stratified flow in the vicinity of a submarine canyon, *Dyn. Atmos. Oceans*, *31*, 47–72.

Boyer, D. L., J. Sommeria, A. S. Mitrovic, V. K. C. Pakala, S. A. Smirnov, and D. Etling (2006), The effects of boundary turbulence on canyon flows forced by periodic along-shelf currents, *J. Phys. Oceanogr.*, *36*, 813–826.

Cannon, G. A. (1972), Wind effects on currents observed in Juan de Fuca submarine canyon, *J. Phys. Oceanogr.*, *2*, 281–285.

Canuto, V. M., A. Howard, Y. Cheng, and M. S. Dubovikov (2001), Ocean turbulence. Part I: One-point closure model—Momentum and heat vertical diffusivities, *J. Phys. Oceanogr.*, *31*, 1413–1426.

Chapman, D. C. (1985), Numerical treatment of cross-shelf open boundaries in a barotropic coastal ocean model, *J. Phys. Oceanogr.*, *15*, 1060–1075.

Connolly, T. P., B. M. Hickey, S. L. Geier, and W. P. Cochlan (2010), Processes influencing seasonal hypoxia in the northern California Current System, *J. Geophys. Res.*, *115*, C03021, doi:10.1029/2009JC005283.

Connolly, T. P., B. M. Hickey, I. Shulman, and R. E. Thomson (2014), Coastal trapped waves, alongshore pressure gradients, and the California Undercurrent, *J. Phys. Oceanogr.*, *44*, 319–342, doi:10.1175/JPO-D-13-095.1.

Crawford, W. R., and M. A. Peña (2013), Declining oxygen on the British Columbia continental shelf, *Atmos. Ocean*, *51*, 88–103.

Emery, W. J., and R. E. Thomson (2004), *Data Analysis Methods in Physical Oceanography*, 2nd ed., 638 pp., Elsevier Sci., Amsterdam.

Fairall, C. W., E. F. Bradley, J. E. Hare, A. A. Grachev, and J. B. Edson (2003), Bulk parameterization of air-sea fluxes: Updates and verification for the COARE algorithm, *J. Clim.*, *16*, 571–591.

Flather, R. A. (1976), A tidal model of the northwest European continental shelf, *Mem. Soc. R. Sci. Liege*, *10*, 141–164.

Foreman, M. G. G., W. R. Crawford, J. Y. Cherniawsky, R. F. Henry, and M. R. Tarbotton (2000), A high-resolution assimilating tidal model for the northeast Pacific Ocean, *J. Geophys. Res.*, *105*(C12), 28,629–28,651.

Foreman, M. G. G., W. Callendar, A. MacFadyen, B. M. Hickey, R. E. Thomson, and E. Di Lorenzo (2008), Modeling the generation of the Juan de Fuca Eddy, *J. Geophys. Res.*, *113*, C03006, doi:10.1029/2006JC004082.

Freeland, H. J., and K. L. Denman (1982), A topographically controlled upwelling centre off southern Vancouver Island, *J. Mar. Res.*, *40*, 1069–1093.

Grantham, B. A., F. Chan, K. J. Nielsen, D. Fox, J. A. Barth, A. Huyer, J. Lubchenco, and B. A. Menge (2004), Upwelling-driven nearshore hypoxia signals ecosystem and oceanographic changes in the northeast Pacific, *Nature*, *429*, 749–754.

Haugerud, R. A. (2000), Digital elevation model (DEM) of Cascadia, latitude 39N–53N, longitude 116W–133W, *Open File Rep. 99-369*, U.S. Geol. Surv., Menlo Park, Calif.

Hickey, B., S. Geier, N. Kachel, and A. MacFadyen (2005), A bi-directional river plume: The Columbia in summer, *Cont. Shelf Res.*, *25*, 1631–1656.

Hickey, B., A. MacFadyen, W. Cochlan, R. Kudela, K. Bruland, and C. Trick (2006), Evolution of chemical, biological, and physical water properties in the northern California Current in 2005: Remote or local wind forcing?, *Geophys. Res. Lett.*, *33*, L22S02, doi:10.1029/2006GL026782.

Hickey, B. M. (1979), The California Current System—Hypotheses and facts, *Prog. Oceanogr.*, *8*, 191–279.

Hickey, B. M. (1989), Patterns and processes of circulation over the Washington continental shelf and slope, in *Coastal Oceanography of Washington and Oregon*, edited by M. R. Landry and B. M. Hickey, pp. 41–115, Elsevier, Amsterdam.

Hickey, B. M. (1997), The response of a steep-sided, narrow canyon to time-variable wind forcing, *J. Phys. Oceanogr.*, *27*, 697–726.

Hickey, B. M. (1998), Coastal oceanography of western North America from the tip of Baja California to Vancouver Island, in *The Sea*, vol. *11*, edited by A. R. Robinson and K. H. Brink, pp. 345–393, John Wiley, New York.

Hickey, B. M., and N. S. Banas (2008), Why is the northern end of the California Current System so productive?, *Oceanography*, *21*(4), 90–107.

Howatt, T. M., and S. E. Allen (2013), Impact of the continental shelf slope on upwelling through submarine canyons, *J. Geophys. Res.*, *118*, 5814–5828, doi:10.1002/jgrc.20401.
Jordi, A., G. Basterretxea, A. Orfila, and J. Tintoré (2006), Analysis of the circulation and shelf-slope exchanges in the continental margin of the northwestern Mediterranean, *Ocean Sci.*, *2*, 173–181.
Kämpf, J. (2007), On the magnitude of upwelling fluxes in shelf-break canyons, *Cont. Shelf Res.*, *27*, 2211–2223.
Kämpf, J. (2009), On the interaction of time-variable flows with a shelfbreak canyon, *J. Phys. Oceanogr.*, *39*, 248–260.
Kämpf, J. (2010), On preconditioning of coastal upwelling in the eastern Great Australian Bight, *J. Geophys. Res.*, *115*, C12071, doi:10.1029/2010JC006294.
Kara, A. B., C. N. Barron, P. J. Martin, L. F. Smedstad, and R. C. Rhoades (2006), Validation of interannual simulations from the 1/8 degree global Navy Coastal Ocean Model (NCOM), *Ocean Modell.*, *11*, 376–398.
Klinck, J. M. (1996), Circulation near submarine canyons: A modeling study, *J. Geophys. Res.*, *101*(C1), 1211–1223.
Kosro, P. M., W. T. Peterson, B. M. Hickey, R. K. Shearman, and S. D. Pierce (2006), Physical versus biological spring transition: 2005, *Geophys. Res. Lett.*, *33*, L22S03, doi:10.1029/2006GL027072.
Landry, M. R., J. R. Postel, W. K. Peterson, and J. Newman (1989), Broad-scale distributional patterns of hydrographic variables on the Washington shelf, in *Coastal Oceanography of Washington and Oregon*, edited by M. R. Landry and B. M. Hickey, pp. 1–40, Elsevier.
Liu, Y., P. MacCready, B. M. Hickey, E. P. Dever, P. M. Kosro, and N. S. Banas (2009), Evaluation of a coastal ocean circulation model for the Columbia River plume in summer 2004, *J. Geophys. Res.*, *114*, C00B04, doi:10.1029/2008JC004929.
MacCready, P. (2011), Calculating estuarine exchange flow using isohaline coordinates, *J. Phys. Oceanogr.*, *41*, 1116–1124.
MacFadyen, A., and B. M. Hickey (2010), Generation and evolution of a topographically linked, mesoscale eddy under steady and variable wind-forcing, *Cont. Shelf Res.*, *30*, 1387–1402.
MacFadyen, A., B. M. Hickey, and W. Cochlan (2008), Influences of the Juan de Fuca Eddy on circulation, nutrients, and phytoplankton production in the northern California Current System, *J. Geophys. Res.*, *113*, C08008, doi:10.1029/2007JC004412.
Marchesiello, P., J. C. McWilliams, and A. Shchepetkin (2001), Open boundary conditions for long-term integration of regional oceanic models, *Ocean Modell.*, *3*, 1–20.
Mass, C. F., et al. (2003), Regional environmental prediction over the Pacific Northwest, *Bull. Am. Meteorol. Soc.*, *84*, 1353–1366.
Mirshak, R., and S. E. Allen (2005), Spin-up and the effects of a submarine canyon: Applications to upwelling in Astoria Canyon, *J. Geophys. Res.*, *110*, C02013, doi:10.1029/2004JC002578.
North, E. W., Z. Schlag, R. R. Hood, M. Li, L. Zhong, T. Gross, and V. S. Kennedy (2008), Vertical swimming behavior influences the dispersal of simulated oyster larvae in a coupled particle tracking and hydrodynamic model of Chesapeake Bay, *Mar. Ecol. Prog. Ser.*, *359*, 99–115.
Rivas, D., and R. M. Samelson (2011), A numerical modeling study of the upwelling source waters along the Oregon coast during 2005, *J. Phys. Oceanogr.*, *41*, 88–112.
Shchepetkin, A. F., and J. C. McWilliams (2005), The regional oceanic modeling system (ROMS): A split-explicit, free-surface, topography-following-coordinate oceanic model, *Ocean Modell.*, *9*, 347–404.
She, J., and J. M. Klinck (2000), Flow near submarine canyons driven by constant winds, *J. Geophys. Res.*, *105*(C12), 28,671–28,694.
Shulman, I., J. C. Kindle, S. deRada, S. C. Anderson, B. Penta, and P. J. Martin (2003), Development of a hierarchy of nested models to study the California Current system, in *Proceedings of the Eighth International Conference on, Estuarine and Coastal Modeling*, edited by M. L. Spaulding, pp. 74–87, Am. Soc. of Civ. Eng., Reston, Virginia.
Song, Y., and D. Haidvogel (1994), A semi-implicit ocean circulation model using a generalized topography-following coordinate system, *J. Comput. Phys.*, *115*, 228–244.
Sutherland, D. A., P. MacCready, N. S. Banas, and L. F. Smedstad (2011), A model study of the Salish Sea estuarine circulation, *J. Phys. Oceanogr.*, *41*, 1125–1143.
Thomson, R. E., and M. V. Krassovski (2010), Poleward reach of the California Undercurrent extension, *J. Geophys. Res.*, *115*, C09027, doi:10.1029/2010JC006280.
Thomson, R. E., S. F. Mihály, and E. A. Kulikov (2007), Estuarine versus transient flow regimes in Juan de Fuca Strait, *J. Geophys. Res.*, *112*, C09022, doi:10.1029/2006JC003925.
Tinis, S. W., R. E. Thomson, C. F. Mass, and B. M. Hickey (2006), Comparison of MM5 and meteorological buoy winds from British Columbia to Northern California, *Atmos. Ocean*, *44*, 65–81.
Umlauf, L., and H. Burchard (2003), A generic length-scale equation for geophysical turbulence models, *J. Mar. Res.*, *61*, 235–265.
Waterhouse, A. F., S. E. Allen, and A. W. Bowie (2009), Upwelling flow dynamics in long canyons at low Rossby number, *J. Geophys. Res.*, *114*, C05004, doi:10.1029/2008JC004956.
Willmott, C. J. (1981), On the validation of models, *Phys. Geogr.*, *2*, 184–194.